博士学位論文

The effects of non-equilibrium angle fluctuation on rotary protein motor kinetics: numerical study with a data driven model
（回転モータータンパク質の反応動力学における角度非平衡揺らぎの効果：データ駆動モデルによる数値解析研究）

田宮 裕治

北海道大学大学院理学院
数学専攻

2018 年 6 月

Abstract

F_1-ATPase is a rotary protein motor whose shaft rotates step-wisely along with intermediate reactions under thermal fluctuation. This protein is intensively studied especially with single molecule measurement in order to reveal its chemo-mechanical coupling mechanism to establish remarkably high energy conversion efficiency. Recent experiments revealed that its chemical reaction rate is modulated by the rotation angle during rotary dwells waiting for the reactions, which suggests that the angle fluctuation plays an important role in the reaction process. Meanwhile, effects of conformational fluctuation on enzyme chemical kinetics have been discussed from both experimental and theoretical view points in other proteins and anomalous kinetics are reported such as non-exponential decay and positive correlation in catalytic turn-over time.

The aim of this study is to scrutinize how the rotary angle fluctuation affects the chemical reaction process of the F_1-ATPase as the temperature changes. Because the single molecule observation can be done only around the room temperature, a mathematical model used in previous works was adopted and extended it to be applicable to a wider range of temperature than is attainable in experiments. This is a one-dimensional model of the rotary angle described by Langevin type stochastic differential equation, where the rotation and rotary dwells are manifested by the brownian motion in harmonic a potential whose bottom position switches stochastically. In order to be consistent with the real data, the model parameter inference is based on objective methods applying statistics and information theory.

As a result of the numerical simulation, the rotary angle distribution during the catalytic dwell was found to deviate from the local-equilibrium one as the temperature increases. This diffusive non-equilibrium property induces two effects which have not been observed in F_1. First, temperature dependence of the rate coefficient of P_i release, one of the fitting exponents of the dwell time distribution, deviates from the Arrhenius law, which has been assumed to hold in experimental estimation of the activation free energy. A modified method is also proposed to calculate the thermodynamic quantities from the static angle dependent rate constant. Second, increasing negative correlation was found as the temperature increases between waiting time for two successive reactions, hydrolysis and P_i release. This breaks the premise of the conventional double-exponential fitting to estimate their rate coefficients and is consistent with the fitting error of simulation data at $60°C > T$, which is close to the physiological temperature of the bacteria which the protein was originally obtained from ($\sim 75°C$). This result proposes a caution against the conventional dwell time analysis when single molecule measurement experiment at such a high temperature becomes possible in the future.

Contents

Chapter 1

Introduction and Background

1.1 F_1-ATPase — Kinetics and Dynamics

1.1.1 Basic Feature

F_1-ATPase is a rotary protein motor and is driven by adenosine triphosphate (ATP), fuel chemical. It consists of the ring-part and the rod part, called $(\alpha\beta)_3$-subunit and γ-subunit, respectively. Every biological cell has this protein and it plays a central roll in metabolism to synthesize ATP in living systems, coupled with another ring-shaped subunit called F_o. ATP has three phosphates (P_i) bound to adenosine and the chemical bond between neighboring phosphates stores large energy (7.3 kcal/mol), which is released when ATP is dissociated into adenosine diphosphate (ADP) and one phosphate. Because one water molecule is consumed during the dissociation, this process is called ATP hydrolysis. The energy released there is used for a wide variety of chemical reactions in other biological molecules and therefore ATP is called the currency of bioenergy. F_1-F_o system is the only enzyme in a living body to synthesize ATP. It utilizes the membrane potential to rotate γ-subunit clockwise through F_o and convert its mechanical energy into the chemical energy to bind ADP and P_i. When F_1 is isolated from F_o, it manifests the reverse reaction; it hydrolyzes ATP into ADP + P_i and rotates γ-subunit counterclockwise by dissociation free energy.

Since this protein has such a large significance in biochemistry, it has been intensively studied for a long time. Especially since the landmarking work by Noji et al. to directly observe its rotation,[1] it is one of the most common biomolecules for single molecule measurement. The prominent feature revealed through their work is that the energy conversion efficiency is close to 100%; in other words, the ATP dissociation free energy was reported to be almost equal to the mechanical rotation energy,[2,3] while only around 30% of thermal energy can be converted into works in macroscopic engines. For this reason, this protein also attracts the physicists' interests.[4–6]

F_1-ATPase has many species with basically same structure and function, among which the one derived from thermophilic *Baccillus* (bacteria) is the most common to be used in rotary assay because of its

stability. In this work, we mention only this type of F_1 (often abbreviated as TF_1) unless we specify the molecular type.

1.1.2 Kinetic Pathways

In order to reveal the mechanism of the highly efficient working principle under fluctuating environment, the kinetic pathway of the catalytic reaction has been intensively studied with single-molecule measurement.

By tethering a fluorescent actin filament or a bead to the γ-subunit, the rotation of the F_1-ATPase can be observed. It generally shows stepwise rotation but the number of the steps depends on the experimental condition such as the time resolution of the measurement, viscosity of the solvent, and the reaction rates. However, it is basically multiple of three because of the three-fold symmetric structure of the $(\alpha\beta)_3$-subunit, where chemical reactions take place to drive the rotation. In other words, the rotary dwell time, the time interval between the steps, corresponds to the waiting time for intermediate reactions. For this reason, the dwell time analysis provides a key to reveal the kinetic pathways, that is, which reaction takes place at which angle. By fitting the dwell time distribution with a multi-exponential function constructed from a kinetic scheme, the "rate constants" of the reactions during the dwell have been obtained.

So far, the size of the step is widely known to be 80° + 40° in maximum and one ATP is consumed every 120° rotation. It was found that the 80° step is driven by ATP binding because the distribution of the dwell time before 80° step is almost single-exponential and its exponent almost linearly depends on the ATP concentration of the solvent.[2] This rotary dwell is called binding dwell. ADP release was later found to take place also at the same angle[7] but its time scale is much shorter than the observation time resolution. On the other hand, hydrolysis (ATP cleavage into ADP + P_i on the catalytic site) and P_i release were found to take place during the dwell before 40° step; the dwell time distribution was almost a double-exponential and one of the exponents has the linear dependence on the P_i concentration of the solvent, while the other timescale was elongated by using a similar substance named ATPγS instead of ATP, which takes longer time to hydrolyze than ordinary ATP.[8] This dwell is called catalytic dwell.

Moreover, it is also studied on which of the three catalytic sites each reaction happens and how many degrees the γ-subunit rotates in 360° unit after the original ATP was bound to the catalytic site. In order to identify the three catalytic sites, fluorescence-labelled ATP (Cy3-ATP)[9] was used and the rotation and the nucleotide (ATP or ADP) state were simultaneously observed.[10] As a result, it was found that ATP is hydrolyzed at 200°[10] and ADP release occurs at 240°,[7] setting the ATP binding angle as 0°. The timing of the P_i release is still controversial but reported to take place at 320° after hydrolysis by the catch-and-release experiment later mentioned.[11] According to this result, the hydrolysis and P_i release take place at different catalytic sites during a catalytic dwell.

1.1.3 Other Recent Topics

1. Temperature sensitive step

At the biding dwell, another reaction was found in addition to ATP binding and ADP release.[12,13] This is called temperature sensitive (TS) step because the temperature dependence of its reaction rate is larger than the other reactions. Because of this temperature dependence, it is difficult to detect at around room temperature. However at lower temperature (around $T < 10°C$), it becomes evident. According to the Arrhenius law (later mentioned), large temperature dependence means large activation free energy and this reaction could be related to the large conformational change and the torque generation.[14]

2. High speed AFM

The high speed atomic force microscopy (AFM) revealed that the rotorless F_1 molecule still shows rotation-like motion with rhythmical open and close motion of the three β subunits although the speed of the "rotation" is slower than that of F_1 with γ-subunit.[15,16] This shows that corporative motion of $(\alpha\beta)_3$-subunit and γ-subunit also enhances the catalytic rate.

3. Small rotation after hydrolysis

During the catalytic dwell, a small rotation was found to take place after hydrolysis by means of data mining approach.[17] The linear fitting of the rotary angle time series during each catalytic dwell shows a positive slope and this is well explained by a Langevin model incorporating a $\sim 20°$ rotation after hydrolysis. This model also supports the reaction order where hydrolysis happens first and P_i release next. In addition to the positive fitting slope, the autocorrelation of the rotary angle during the dwell shows double exponential decay, which cannot be explained by a model without the small rotation during the dwell. Because P_i release is much more sensitive to the rotary angle than hydrolysis, this small angle shift brings the system where P_i is much easier to be released; in other words, hydrolysis was revealed to play a role of a 'key' to 'unlock' P_i release to enhance the correct reaction ordering.

1.2 Rate Constants, Rate Coefficients, and Dwell Time Analysis

1.2.1 What is the Rate Constant?

As shown in the previous section, the rate constant is one of the key quantities to reveal the kinetic pathway of biomolecules. The chemical reaction in a biomolecule in general consists of various elementary chemical reaction processes. Such elementary reactions include the binding or detaching of the chemical substances to catalyze (ligand), electron transfer between the biomolecule and the ligand or within the protein, and small or large protein conformational changes, for example. The biomolecule reaction stands on a hierarchy of various reactions with different spatio-temporal scales. In general, the waiting time of the chemical reaction is considered to obey an exponential function. Under such a situation, the rate constant is the exponent of this waiting time distribution.

As well as this is the measure of the timescale of the chemical reaction, we can also estimate the minimum energy the system needs to induce the reaction, that is, the activation energy E_a. According to the Arrhenius law, the temperature dependence of the rate constants can be expressed as follows;

$$k \propto \exp(-E_a/k_B T). \tag{1.1}$$

k_B, T are the Boltzmann constant and the temperature, respectively. This is an empirical law and known to hold for a wide variety of chemical reaction processes.

Based on the statistical mechanics, a microscopic understanding of this law was attained by Eyring[18] and Evans & Polanyi,[19] called the transition state theory. They considered that the chemical reaction is the transition between a chemical potential well to another, climbing up the energy barrier bridging over the two potentials. The height of this barrier corresponds to the activation energy E_a. The dividing boundary lying between the initial state (reactant) potential and the final state (product) potential is called the transition state. The rate constant is the escape rate from the reactant potential to the product potential. With equilibrium statistical mechanics treatment, they calculated the ratio of the flow at the transition state from the reactant to the product over the the probability to reside in the reactant state, they obtained the rate constant of the reaction as follows;

$$k = \frac{k_B T}{h} \exp\left(-\frac{E_a}{k_B T}\right), \tag{1.2}$$

where h is the Planck constant.

Later on, the thermodynamic interpretation of this relation was proposed.

$$k = \frac{k_B T}{h} \exp\left(-\frac{\Delta G^\ddagger}{k_B T}\right) \tag{1.3}$$

$\Delta G^\ddagger$ is the (Gibbs') activation free energy. Because chemical reactions in general take place under the isothermal condition and the Gibbs' free energy is related with the enthalpy H and the entropy S as $G = H - TS$, the activation free energy is expressed as $\Delta G^\ddagger = \Delta H^\ddagger - T\Delta S^\ddagger$, where $\Delta H^\ddagger, \Delta S^\ddagger$ are the activation enthalpy and entropy. Using this relationship, eqn(1.3) can be rewritten as

$$k = \frac{k_B T}{h} \exp\left(\frac{\Delta S^\ddagger}{k_B}\right) \exp\left(-\frac{\Delta H^\ddagger}{k_B T}\right). \tag{1.4}$$

Comparing it with eqn(1.2), the activation enthalpy $\Delta H^\ddagger$ corresponds to the barrier height and the activation entropy $\Delta S^\ddagger$ to the difference in the phase space volume between the reactant potential and the transition state, which can be understood as the width of the reactant potential when the system can be projected onto one-dimension.

1.2.2 Dwell Time Analysis to Obtain the "Rate Constants"

In the single-molecule studies of F_1-ATPase, "rate constants" have been experimentally obtained from the rotary dwell time analysis. Because the rotary dwell can be understood as the waiting time for the intermediate reactions, the dwell time distribution is expected to have the exponents which correspond to their rate constants. For example at catalytic dwell, a double-exponential function is often used for simplicity based on the reaction scheme that hydrolysis and P_i release take place successively, neglecting the backward reactions, ATP synthesis and P_i rebinding. In this case, the fitting function can be obtained from the convolution of the two exponential functions;

$$P_{1,2}(\tau) = \int_0^\tau \int_0^\tau \delta(\tau - (\tau_1 + \tau_2)) P_1(\tau_1) P_2(\tau_2) d\tau_1 d\tau_2 \tag{1.5a}$$

$$= \int_0^\tau k_1 e^{-k_1\tau_1} k_2 e^{-k_2(\tau-\tau_1)} d\tau_1 \tag{1.5b}$$

$$= \frac{k_1 k_2}{k_1 - k_2} \left(e^{-k_2\tau} - e^{-k_1\tau} \right), \tag{1.5c}$$

Its survival distribution $S(\tau) = 1 - \int_0^\tau P(\tau')d\tau'$ is;

$$S_{1,2}(\tau) = \frac{k_1 k_2}{k_1 - k_2} \left(e^{-k_2\tau}/k_2 - e^{-k_1\tau}/k_1 \right). \tag{1.6}$$

Although this fitting method is quite often adopted, we must remark here that there are two assumptions. First one is that the waiting time for the waiting time distribution for each intermediate reaction is single-exponential. The second one is that the waiting time of the two reactions are independent of each other. So far in experiments, almost no careful attention is paid to the validities of these assumptions because the double-exponential fitting goes well under the temperature around $15 \sim 30°\mathrm{C}$.

1.2.3 Angle-dependent Rate Constant

Recently, a new aspect of the rate constants was revealed by trapping experiments with magnetic tweezers.[11,20] The rate constants of the intermediate reactions were found to depend on the rotary angle. A magnetic bead was attached to the γ-subunit and the rotation was arrested by the magnetic field at certain angle for a while. If the reactions take place during the arrest, the γ-subunit goes on to the equilibrium position of the next dwell after the magnetic field is cut off while it goes back to the equilibrium position of the current dwell if the reactions are not completed. Repeating this catch-and-release process for many times, the probability $P_\mathrm{f}(t)$ of whether the γ-subunit rotates forward or backward after the arrest was measured for different arresting time t. Fitting this function with a model function constructed by assuming a kinetic scheme during the arrest, the rate constants of the intermediate reactions at a fixed arrested angle were estimated. This result shows that the reaction and the rotation are intimately coupled and suggests that how the rotary angle fluctuates during a dwell also affects the dwell time. In other words, the dwell time fitting exponents, which have been called "rate constants", are affected by the mechanical fluctuation of the protein conformation. Actually, the friction dependence of the $\mathrm{P_i}$ release "rate constant" obtained by the dwell time analysis was well explained by this angle-dependent rate constants and the change in the rotary angle fluctuation, utilizing a mathematical model reflecting this chemo-mechanical coupling picture.[21] In order to make a clear distinction from the angle-dependent rate constants, from now on we call these quantities as "rate coefficients" and denote them as $\bar{k}_i$.

In this research, we take a closer look at the relationship between the enzyme kinetics and the conformational fluctuation.

1.3 Brownian Motion and Fluctuating Enzymes

Because proteins work in a nano-scale world, the thermal fluctuation cannot be neglected. In modeling their behavior, mathematical tools for Brownian motion is sometimes adopted. In this section, we give a brief explanation of the Langevin and Fokker-Planck equation to describe Brownian dynamics and review protein dynamics studies based on these formalisms.

1.3.1 General Description of Brownian Motion

Brownian motion was first found by Robert Brown from grains inside pollens in water.[22] Its cause was theoretically investigated by the pioneering work by Albert Einstein[23,24] and experimentally verified by Jean Perrin.[25,26]

A trajectory of Brownian motion is completely random; it changes the direction every time without correlation. Consider that $X(t)$ is a trajectory of Brownian motion. Its spatial displacement after time Δt, that is, $\Delta X(t) = X(t + \Delta t) - X(t)$, is independent and identically distributed Markov process and its average is 0. It does not depend on the time t, either. Moreover, its standard deviation increases with square root of time displacement on average; $\sqrt{\mathbb{E}[(\Delta X(t))^2]} \propto \sqrt{\Delta t}$, where $\mathbb{E}[\cdot]$ is the ensemble average. Especially, the probability distribution $P(\Delta X; \Delta t)$ of $\Delta X(t)$ was Gaussian;

$$P(\Delta X; \Delta t) = \frac{1}{\sqrt{\pi C \Delta t}} \exp\left\{-\frac{(\Delta X)^2}{C\Delta t}\right\}, \tag{1.7}$$

where C is a constant magnifying the speed of the motion. Later, it was summed up as Wiener process $B(t)$ as bellow;

$$\mathbb{E}[B(t)] = 0, \tag{1.8a}$$
$$\mathbb{E}[B(t_1)B(t_2)] = \min(t_1, t_2). \tag{1.8b}$$

The second relationship includes the linear time evolution of the mean square displacement

$$\mathbb{E}[B(t)^2] = t, \tag{1.9}$$

and the independence of the spatial displacement

$$\mathbb{E}[\{B(t_1) - B(t_2)\}\{B(t_3) - B(t_4)\}] = 0 \tag{1.10}$$

if the time intervals (t_1, t_2) and (t_3, t_4) have no overlap.

1.3.2 Langevin Equation for Each Brownian Trajectory

In order to describe the detailed dynamics of the Brownian motion in physics, Langevin equation[27–31] was first introduced by P. Langevin.[32,33]

$$m\frac{d^2x(t)}{dt^2} = -\eta\frac{dx(t)}{dt} - \frac{dU(x)}{dx} + \sqrt{2D}\xi(t). \tag{1.11}$$

This Newtonian equation of motion describes a trajectory of a Brownian particle under a potential $U(x)$. The first term in the right hand side $-\eta\frac{dx}{dt}$ is the frictional force due to the surrounding media. If the ratio of the mass m and the friction constant η is much smaller than the observation timescale $m/\eta << \tau_{\rm ob}$, the inertia can be neglected and we can omit the second derivative term;

$$\eta\frac{dx(t)}{dt} = -\frac{dU(x)}{dx} + \sqrt{2D}\xi(t). \tag{1.12}$$

It is called overdamped limit and in general verified in describing protein dynamics (details are in Appendix A.1.1).

$\xi(t)$ is a Gaussian random white noise and corresponds to the time derivative of a Wiener process $\xi(t) = \frac{dB(t)}{dt}$ although this $B(t)$ is actually not differentiable. Because of the properties above (1.8), this white noise has these properties

$$\langle\xi(t)\rangle = 0, \tag{1.13a}$$
$$\langle\xi(0)\xi(t)\rangle = \delta(t). \tag{1.13b}$$

$\langle\cdot\rangle$ represents the ensemble average over every possible noise realization. Eqn.(1.13a) means the direction (+ or −) and size of the noise has no bias and eqn.(1.13b) means that the noise size and direction is independent at different time. We remark that if we write the random noise as $F(t) = \sqrt{2D}\xi(t)$, its correlation function is $\langle F(0)F(t)\rangle = 2D\delta(t)$

It is sometimes wrongly understood that the random force term $\sqrt{2D}\xi(t)$ is the collisional force of the surrounding molecules to the Brownian particle. It is partly true but the frictional force term $-\eta\frac{dx}{dt}$ also originates from the collision. The random force is the mean force due to the molecular collision forces averaged within a mesoscopic timescale. Because both random force and frictional force terms share the same origin, there is an important relation between the friction constant η and the diffusion constant D called the fluctuation dissipation relation. When the thermal equilibrium is attained between the surrounding media and the Brownian particle, the relation below holds;

$$D = \eta k_B T. \tag{1.14}$$

k_B and T are the Boltzmann constant and the temperature, respectively.

1.3.3 Special Case: Ornstein-Uhlenbeck Process

When there is no potential, the underdamped Langevin equation (eqn.(1.11)) is

$$m\frac{du(t)}{dt} = -\eta u(t) + \sqrt{2D}\xi(t), \tag{1.15}$$

where $u(t) = dx(t)/dt$ is the velocity. Meanwhile, the Brownian motion under a harmonic potential $U(x) = \frac{1}{2}kx^2$ in the overdamped limit is

$$\eta\frac{dx(t)}{dt} = -kx(t) + \sqrt{2D}\xi(t). \tag{1.16}$$

These two elementary processes have the same mathematical structure and called the Ornstein-Uhlenbeck (O.-U.) process. The important properties in the O.-U. process are that the average, the standard

deviation, and the autocorrelation function can be easily obtained in simple forms. Especially, taking the overdamped limit with a harmonic potential as an example the autocorrelation function is as follows;

$$\langle x(t)x(t')\rangle = \frac{k_BT}{k}e^{-\frac{k}{\eta}|t-t'|}. \tag{1.17}$$

Here, the thermal equilibrium and the fluctuation dissipation relation (eqn.(1.14)) are assumed at any time instant so that $k\langle x(t)^2\rangle/2 = k\langle x(0)^2\rangle/2 = k_BT/2$. This relation shows that the memory of the trajectory decays with a time constant $\tau_{\rm rel} = \eta/k$. We use this relationship later in the parameter estimation of a molecular motor model.

In addition, the average and (square of) the standard deviation are as follows;

$$\langle x(t)\rangle = \langle x(0)\rangle e^{-\frac{k}{\eta}t} \xrightarrow{t\to\infty} 0, \tag{1.18a}$$

$$\langle x(t)^2\rangle - \langle x(t)\rangle^2 = \frac{D}{\eta k}\left(1 - e^{-\frac{2k}{\eta}t}\right) \xrightarrow{t\to\infty} \frac{D}{\eta k} = \frac{k_BT}{k}. \tag{1.18b}$$

The mathematical details are in Appendix A.1.2.

1.3.4 Fokker-Planck Equation for Ensemble Behavior

While the Langevin equation describes a single trajectory of the Brownian motion, its ensemble behavior is described by the Fokker-Planck equation, a time propagation equation of the distribution function. Given a general form of the Langevin equation

$$dX(t) = a(X,t)dt + b(X,t)dB(t), \tag{1.19}$$

the corresponding Fokker-Planck equation is

$$\frac{\partial P(X;t)}{\partial t} = -\frac{\partial}{\partial X}\left\{a(X,t)P(X;t)\right\} + \frac{1}{2}\frac{\partial^2}{\partial X^2}b(X,t)^2P(X;t). \tag{1.20}$$

$P(X;t)$ is the probability distribution of X at time t. The derivation is in Appendix A.1.3. The first term of the right hand side is the derivative of the flux, $a(X,t)P(X;t)$, which is caused by the potential force or the external force. The second term causes the diffusive motion induced by the random force. Especially, the Langevin equation with overdamped limit corresponds to

$$\frac{\partial P(x;t)}{\partial t} = -\frac{\partial}{\partial x}\left\{-\frac{1}{\eta}\frac{dU(x)}{dx}P(x;t)\right\} + \frac{D}{\eta^2}\frac{\partial^2}{\partial x^2}P(x;t), \tag{1.21}$$

which is called Smolchowski equation. In this case, the stationary solution $P_{\rm st}(x)$ can be easily obtained with boundary conditions $P_{\rm st}(x) \xrightarrow{x\to\pm\infty} 0$ and $\frac{\partial P_{\rm st}(x)}{\partial t} \xrightarrow{x\to\pm\infty} 0$;

$$\begin{aligned} P_{\rm st}(x) &= \frac{1}{Z}\exp\left\{-\frac{\eta}{D}U(x)\right\} \\ \text{where}\quad Z &= \int_{-\infty}^{\infty}\exp\left\{-\frac{\eta}{D}U(x')\right\}dx'. \end{aligned} \tag{1.22}$$

It coincides with the Maxwell-Boltzmann equilibrium distribution $\propto \exp\left\{-\frac{U(x)}{k_BT}\right\}$ if we assume the fluctuation dissipation relation (eqn.(1.14)).

Now we consider the relaxation process toward the equilibrium distribution with a fixed initial condition $x(0) = x_0$, which means $P(x; t = 0) = \delta(x - x_0)$. Its time evolution can be relatively easily obtained in the Ornstein-Uhlenbeck process. The Fokker-Planck equation of the Ornstein-Uhlenbeck process is

$$\frac{\partial P(x;t)}{\partial t} = -\frac{\partial}{\partial x}\left\{-\frac{k}{\eta}xP(x;t)\right\} + \frac{k_BT}{\eta}\frac{\partial^2}{\partial x^2}P(x;t). \tag{1.23}$$

Solving this equation, we obtain;[27]

$$P(x;t) = \sqrt{\frac{k}{2k_BT(1-e^{-\frac{2k}{\eta}t})}}\exp\left\{-\frac{k(x-x_0e^{-\frac{k}{\eta}t})^2}{2k_BT(1-e^{-\frac{2k}{\eta}t})}\right\} \xrightarrow{t\to\infty} \sqrt{\frac{k}{2k_BT}}\exp\left(-\frac{kx^2/2}{k_BT}\right) \tag{1.24}$$

It shows that the probability distribution asymptotically approaches the Maxwell-Boltzmann distribution for any initial distribution. Moreover, its characteristic timescale is $\tau_{\rm rel} = \eta/k$.

1.3.5 Reaction-Diffusion Formalism for Enzyme Kinetics: Disperse Kinetics and Dynamic Disorder

Using the mathematical formalism described in the previous subsections, the relation between the enzyme conformation fluctuation and the chemical reactions has been discussed since 1980's. The initiative work would be Agmon and Hopfield's theoretical study on CO rebinding to Heme-protein.[34,35] In experiments, the CO bound to Heme was dissociated by laser pulse and the rebinding process was measured, showing that the decay rate of the unbound Heme is non-exponential and that this decaying dynamics is affected by the viscosity of the media.[36] In order to explain this anomalous kinetics and viscosity dependence deviating from the Kramers' theory,[37] they added a phenomenological coordinate X manifesting the protein conformational fluctuation perpendicular to the intrinsic reaction coordinate and introduced a one-component rate equation of the unbound Heme concentration $C(X)$ whose rate constant $k(X)$ depends on the enzyme conformation fluctuation described by a Brownian motion in a harmonic potential (O.-U. process);

$$\frac{dC(X)}{dt} = -k(X)C(X), \tag{1.25a}$$

$$\frac{dX(t)}{dt} = -\lambda X(t) + \sqrt{2\lambda k_BT}\xi(t). \tag{1.25b}$$

$X(t)$ corresponds to the conformational motion of the protein which is continuously opening and closing and λ is the equilibrium relaxation rate of the protein conformation. Considering that the rate constant of the reaction changes with the conformation, the rate constant depends on $X(t)$; especially in their study, they assumed an exponential dependence

$$k(X) = A\exp(-\alpha X), \tag{1.26}$$

where A and α are constants. If $\alpha \propto 1/k_BT$, this dependence can be interpreted as due to the linearly-X-dependent activation free energy. The formal solution of this equation is as follows;

$$C(t) = C(0)\exp\left\{-\int_0^t k(X(s))ds\right\}. \tag{1.27}$$

While it becomes single exponential decay $C(t) = e^{-kt}$ if the rate constant $k(X)$ does not depend on X, the actual decaying process depends on the Brownian motion of X. In order to understand it more clearly, we transform eqn.(1.25) into an equivalent partial differential equation of the concentration $\bar{C}(X;t)$ at conformational coordinate X;

$$\frac{\partial \bar{C}(X;t)}{\partial t} = -k(X)\bar{C}(X;t) - \frac{\partial}{\partial X}\left\{-\lambda X \bar{C}(X;t)\right\} + \lambda k_B T \frac{\partial^2}{\partial X^2}\bar{C}(X;t). \tag{1.28}$$

This is called Agmon-Hopfield equation and can be easily understood as adding the reaction term $-k(X)\bar{C}(X;t)$ to the Fokker-Planck equation of the O.-U. process (eqn.(1.23)) and we can say that this system is within a reaction-diffusion formalism. While the conformation $X(t)$ approaches the equilibrium distribution $P(X) \propto \exp(-X^2/2k_BT)$ with the characteristic timescale $\tau_{\rm rel} = 1/\lambda$ in the same way as the previous subsection, the concentration $\bar{C}(X;t)$ decreases at each coordinate X with a rate $-k(X)\bar{C}(X;t)$.

The concentration of the unbound Heme $C(t)$ can be obtained by integrating the solution of eqn.(1.28) over X, that is, $C(t) = \int \bar{C}(X;t)dX$. Because this system has two timescales for the conformational relaxation and the chemical reaction and these two processes are coupled through the rate constant $k(X)$, the decaying process of the unbound Heme concentration $C(t) = \int \bar{C}(X;t)dX$ is affected by the relationship between these timescales. In order to understand it intuitively, we take two extreme cases as examples.

- Static disorder

  When the reaction timescale is shorter than the diffusion timescale of X over the potential, the decaying dynamics only depends on the initial condition of X at $t = 0$ because the reaction takes place before the relaxation process of X begins;

  $$C(t) = C(0)\int \exp\left\{-k(X)t\right\} P(X;t=0)dX. \tag{1.29}$$

- Fast diffusion limit

  When the diffusion timescale is shorter than that of the reaction timescale, there is enough time to relax into the equilibrium state in the potential before the chemical reaction takes place. In this case, regardless of the initial condition of X, the time evolution of the concentration $C(t)$ decays single exponentially as

  $$C(t) = C(0)\exp(-\langle k\rangle_{\rm eq} t), \tag{1.30}$$

  with the overall rate constant averaged over the equilibrium ensemble;

  $$\int_0^t k(X(s))ds = \left\{\frac{1}{t}\int_0^t k(X(s))ds\right\} t \approx \left\{\int k(X)P_{\rm eq}(X)dX\right\} t. \tag{1.31}$$

The point is that the kinetics changes depend on the relationship between two timescales: the chemical reaction timescale and the diffusion (or equilibrium relaxation) timescale. When the diffusion timescale is short enough compared with the chemical reaction, the equilibrium relaxation process of the conformation can be neglected and the decaying of the unbound Heme concentration is single-exponential with the rate

constant $\langle k \rangle_{\rm eq}$. On the other hand, when the diffusion is too slow compared with the reaction timescale, the protein conformation can be regarded as "frozen" while waiting for the reaction. The time evolution of the concentration $C(t)$ is affected by the initial condition of the conformation and on average it has various exponents. In the intermediate case when the reaction and diffusion timescales are comparable, the reaction takes place before the memory of the initial condition is completely lost and we can expect non-exponential decaying process.

Agmon and Hopfield considered that the non-exponential decaying of the unbound Heme protein is due to the multiple reaction pathways affected by the non-equilibrium conformational fluctuation induced by the timescale competition.

This can be generalized into the discrete kinetics case. When the protein can take multiple numbers of conformations before the chemical reaction happens, the whole kinetics can be described by the Markov chain network. If each conformation has a different rate constant, the waiting time for the chemical reaction can be affected by the transition timescale among the conformations. Actually, the kinetics with continuous conformational change in Agmon-Hopfield model can also be transformed into this discrete kinetics by time-discretization.

This mechanism of the disperse kinetics was applied to other fields (e.g. the electron transportation kinetics of a protein, Sumi-Marcas theory [38]) and called dynamic(al) disorder. [39] Around 2000's, the single molecule measurement technology was developed and it became possible to directly observe the enzyme turnover kinetics. Labelling cholesterol oxidase molecules by fluorescent dyes, S. Xie group succeeded in detecting the non-exponential kinetics in the turnover time distribution. [40–42] They also found that the successive turnover time was positively correlated and tried to explain it within the similar framework as the Agmon-Hopfield kinetics. [43] They considered that the enzyme can take several different conformations before the ligand binding and that some of them are more reactive than the others (in other words, have larger rate constants). When the ligand concentration is high enough and the ligand binding timescale is comparable with that of the conformation transition, the protein can continue to take the same conformation and the turnover time does not change so much. [44,45] Although their theoretical model can not fully explain the diagonal positive correlation on the two-body correlation plot, an improved model by Mikhaelov group succeeded in reproducing it. [46]

In these ways, the coupling between the conformational fluctuation and the reaction rates has been intensively discussed to explain the anomalous kinetics of proteins. As the rate constants of the reactions are coupled with the rotary angle of the F_1-ATPase, such behaviors could also be observed in protein motor systems. On the other hand, there are skeptical views on the dynamic disorder that such phenomena could have arisen from the artifacts in analysis of the experimental data. [47] The change of the intensity of the fluorescence can be indistinguishable with the noise due to the thermal fluctuation or diffraction in observation. In such a low signal-to-noise (S/N) ratio data, the rapid fluctuation of the noise can be detected as the change point and many short time series segments come out successively and regarded as turnover time, producing an artificial positive correlation. Actually, a case is reported that the correlation disappeared by introduction of an objective change point detection method. So far the dynamic disorder models were discussed to explain the experimental results although doubts are shed against their reliability. Proposing the experimental verification based on the model simulation approach

is expected to reinforce the plausibility of this phenomenon. In this sense, F_1-ATPase is a good target to study.

1.4 Purpose of this Study

In this study we focus on the effect of the fluctuation on the chemical kinetics of F_1-ATPase. Because of the chemo-mechanical coupling through the rotary-angle-dependent rate constant, we can expect the emergence of the disperse kinetics when the rotary angle diffusion timescale gets short relative to the reaction timescale. In order to realize such situation, there are three possible quantities to change;

- Friction
  As was done by R. Watanabe et al.,[21], the diffusion timescale can be changed by attaching rotation probes with different effective friction constants (different size, material, shape) to the γ-subunit.

- Reaction rate
  Some of the reaction rates can be continuously modulated to some extent. The ATP binding rate constant is dependent on its concentration in the solvent linearly. The P_i release rate constant itself is difficult to manipulate but by changing the its concentration the net rate can be changed through the rebinding.[7]

- Temperature
  Both diffusion and reaction timescales are affected by temperature. Based on the Arrhenius picture, the chemical reaction is accelerated by increasing the temperature. The viscosity of the solvent also decreases at high temperature in general and the mobility of the γ-subunit can be enhanced.

Among them, we take a look at the effect of the temperature in this work.

As to the temperature, the F_1-ATPase widely studied in experiments are derived from thermophilic *Bacillus* (bacteria), whose physiological temperature is around 75°C although single molecule measurements are usually done at room temperature. The highest temperature reported so far is 40°C[48] and it is difficult to observe the molecule at temperature higher than that because of the experimental settings (e.g. the durability of the camera lens and the molecular attachment to the cover glass surface). From the temperature dependence of the rate coefficient, the activation free energy of the intermediate reactions are estimated assuming the Arrhenius law.[14,49] However, the rate coefficient obtained from the dwell time analysis not only depends on the activation free energy but also on the rotary angle fluctuation because of the chemo-mechanical coupling. Due to the disperse kinetics, non-obvious temperature dependence could appear and affect the result of the experiments. Actually, the breakdown of the Arrhenius relation is expected from theoretical view points.[34,50]

In order to elucidate how the rotary angle fluctuation changes with temperature and affects the kinetics of the F_1-ATPase, especially the temperature dependence of the rate coefficients and the correlation in the time waiting for the reaction. Because the essential factor to induce the disperse kinetics is the intimate

coupling of the conformation and the reactivity, we focus on the catalytic dwell, where the angle-sensitive P_i release takes place. We adopted a potential switching model used in the experiment-based studies [17,21] and extended it so as to be applicable to a wide range of temperature. In order to be faithful to the reality, we tuned the model parameters from the time series analysis of the experimental data, the single molecule rotary assay around room temperature. From the extrapolative simulation study with the model, we investigated the rate coefficients and the reaction time correlation of the hydrolysis and P_i release steps at higher and lower temperature than room temperature, which is unaccessible within the current technology of the single molecule observation.

Chapter 2

Model Settings and Data Analysis

2.1 Experimental Data

2.1.1 Details of the Data

First of all, the experimental data we analyze to make a mathematical model is provided by Prof. Noji and Dr. Watanabe in the University of Tokyo, the same data as was investigated in R. Watanabe et al. (2013).[21] The data sets are obtained under the condition below;

- A gold nano particle with 80nm diameter is attached to the γ-subunit as a rotary probe
- High time resolution with 27000 frames per second (fps)
  In this condition, the catalytic dwell can be detected with the wild type F_1 molecule.
- High ATP concentration (200μM)
  In this condition, the ATP binding dwell is too short to observe with the time resolution above.
- Four different temperature at 16, 20, 25, 33°C
  From the temperature difference of the analysis result, we extract a physical quantity which corresponds to the activation free energy (Sec.2.4.2).

Due to the first and second conditions, we can concentrate only on the catalytic dwells at $T \geq 20$°C. Because the catalytic dwell contains the angle sensitive P_i release step, it meets with our motivation to elucidate the chemo-mechanical coupling effect. For 16°C data, however, the ATP binding dwells are also detected because of the temperature sensitive step and so we have to select out catalytic dwells and binding dwells (see Sec.2.3.3)

The experimental time series data we received are as below (see also Fig.2.1);

- the rotary trace (the (X, Y) coordinate of the probe bead detected above by microscopy)
- the rotary angle (two types : the one with 360° unit and the accumulative one)

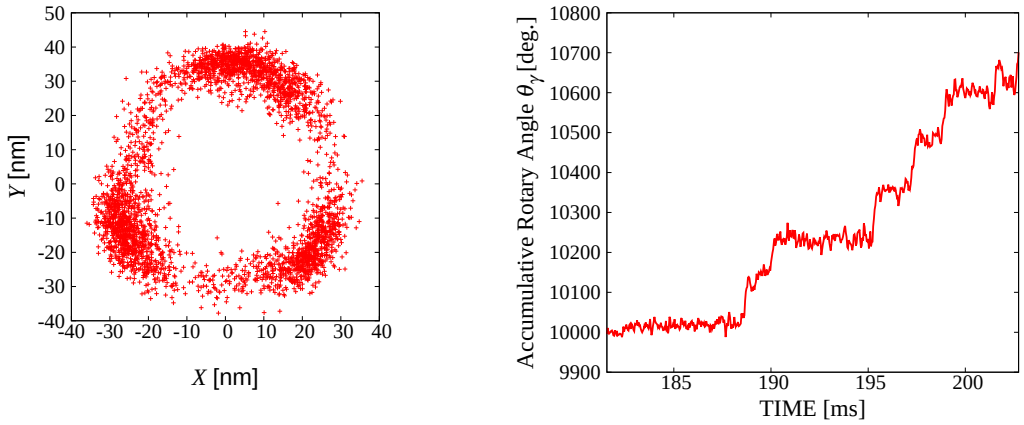

(a) (b)

Fig.2.1: A sample of the experimental data (25°C). (a) The rotary trace of the probe bead attached to the γ-subunit observed from above. The rotation center is set as the origin of the coordinate. (b) The accumulative rotary angle of the γ-subunit obtained from the rotary trace. Because of the experimental conditions mentioned above, it is 120° stepwise with catalytic dwells.

The rotary angle is given in advance from the rotation center (X_0, Y_0) ($(0,0)$ in Fig2.1(a)) assigned by the experimentalists. However, when the rotary center seemed to shift during the rotation, we reassigned the rotation center for short time intervals and applied polynomial fitting to obtain the time-dependent rotation center.

We made a mathematical model based on this experimental setting and tuned the physical parameters.

2.2 Potential Switching Model

2.2.1 General Description

In order to theoretically investigate the dynamics and kinetics of the F_1-ATPase, a one-dimensional potential switching model[51,52] is often adopted, taking the rotary angle θ of the γ shaft as the coordinate. The basic properties of the model are as below;

- the rotary dwell waiting for a chemical reaction is described as the Brownian motion in a potential
- the rotation is described by the stochastic shift of the potential

The harmonic potential reflects the elastic force exerted to the γ-subunit due to the conformational deformation of the $(\alpha\beta)_3$-subunit. The switching of the potential corresponds to the conformational change of the $(\alpha\beta)_3$-subunit induced by chemical reactions. A simple mathematical manifestation of this setting is as follows;[52]

$$\frac{\partial P_i(\theta;t)}{\partial t} = -\frac{\partial}{\partial\theta}\left\{-\frac{1}{\Gamma}\frac{dU_i(\theta)}{d\theta}P_i(\theta;t)\right\} + \frac{k_BT}{\Gamma}\frac{\partial^2}{\partial\theta^2}P_i(\theta;t) + \sum_j^N \left\{k_{j\to i}P_j(\theta;t) - k_{i\to j}P_i(\theta;t)\right\}. \quad (2.1)$$

Γ is the effective friction constant of the revolving rotation probe. The number of dwells is assumed to be N and $P_i(\theta;t)$ is the rotary angle distribution in the ith dwell at time t. Quite similarly to the Agmon-Hopfield model (eqn.(1.28)), the term representing the discrete transition between states (the third term of the right hand side of eqn(2.1)) is added to the Smolchowski equation. $k_{i\to j}$ is the rate constant of the transition from the ith state (dwell) to the jth state (dwell). The remarkable differences from the Agmon-Hopfield model are that it can take multiple states ($i = 1, 2, ..., N$) and that the incoming transition $k_{j\to i}P_j(\theta;t)$ is also taken into account. Because of these properties, the total probability $P_{\rm sum}(\theta;t) = \sum_i^N P_i(\theta;t)$ can be conserved contrary to the Agmon-Hopfield model, where the concentration $\bar{C}(x;t)$ decays with time. In this case, the probability distribution $P_i(\theta;t)$ approaches the steady state distribution $P_i^{\rm st}(\theta)$ with time, which is the solution of eqn.(2.1) with zero time-derivative $\frac{\partial P_i(\theta;t)}{\partial t} = 0$.

2.2.2 Simple Example of Non-equilibrium State

Here, we take a simple example to consider the effect of the incoming transition term;

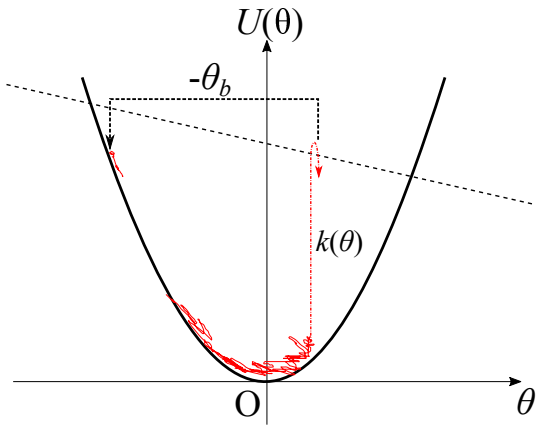

Fig.2.2: The schematic picture of the single potential switching model. A trajectory in Brownian motion escapes from a potential $U(\theta)$ with an angle-dependent rate constant $k(\theta)$ and returns to the same potential with θ_b angle shift. The grey broken line shows the angle-dependent activation free energy barrier, which corresponds to $\Delta G^{\ddagger}(\theta) = -k_BT\log\{hk(\theta)/k_BT\}$.

$$\frac{\partial P(\theta;t)}{\partial t} = -\frac{\partial}{\partial\theta}\left\{-\frac{1}{\Gamma}\frac{dU(\theta)}{d\theta}P(\theta;t)\right\} + \frac{k_BT}{\Gamma}\frac{\partial^2}{\partial\theta^2}P(\theta;t) - k(\theta)P(\theta;t) + k(\theta+\theta_b)P(\theta+\theta_b;t). \quad (2.2)$$

This exactly coincides with the Agmon-Hopfield model (1.28) except for the last term $+k(\theta+\theta_b)P(\theta+\theta_b;t)$. Because of this term, the trajectory escaped from the potential due to the term $-k(\theta)P(\theta;t)$ comes back with the angle shift $-\theta_b$, conserving the probability $P(\theta;t)$ as is simply understood by integrating left and right hand sides of the eqn.(2.2) with θ so that $\frac{\partial}{\partial t}\int P(\theta;t)d\theta = 0$. This type of reinsertion with angle shift is physically plausible in rotary protein motor systems because of the symmetrical structure. For example in the F_1-ATPase, moving to the next catalytic dwell can be represented by reinsertion with 120° if the three catalytic dwells can be regarded as exactly the same.

The steady state distribution of this setting $P_{\rm st}(\theta)$ is obtained by solving

$$0 = -\frac{\partial}{\partial\theta}\left\{-\frac{1}{\Gamma}\frac{dU(\theta)}{d\theta}P_{\rm st}(\theta;t)\right\} + \frac{k_BT}{\Gamma}\frac{\partial^2}{\partial\theta^2}P_{\rm st}(\theta) - k(\theta)P_{\rm st}(\theta) + k(\theta+\theta_b)P_{\rm st}(\theta+\theta_b). \tag{2.3}$$

When the effect of diffusion is dominant and the reaction $k(\theta+\theta_b)P_{\rm st}(\theta+\theta_b)$ can be neglected, this equation coincides with an ordinary Smolchowski equation (eqn.(1.21)) and $P_{\rm st}(\theta)$ is almost close to the equilibrium distribution $P_{\rm eq}(\theta) \propto \exp\left\{-\frac{U(\theta)}{k_BT}\right\}$ as is discussed in Sec.1.3.4. This is called quasi-equilibrium state. On the other hand, $P_{\rm st}(\theta)$ generally deviates from $P_{\rm eq}(\theta)$ when the reaction cannot be neglected. This deviation is brought about because the reaction takes place before the equilibrium relaxation is completed. Here we call this non-equilibrium state. The form of the non-equilibrium steady state distribution $P_{\rm st}(\theta)$ is mainly determined by two properties; the strength of the diffusion (determined by the diffusion constant $D = k_BT/\Gamma$) relative to the reaction (determined by the rate constant $k(\theta)$), and the initial angle distribution $P(\theta;t=0)$.

In all, we can see that the competition between the diffusion timescale and the reaction timescale also plays an important role when the incoming probability exists. When the diffusion is much more rapid than the reaction, the system approaches the quasi-equilibrium state. If the reaction is dominant, the equilibrium relaxation cannot catch up with the potential switching due to the reaction and the non-equilibrium sate appears. This mechanism to produce the diffusive non-equilibrium property can also take place when the number of states (dwells) is more than one.

2.2.3 Model Introduction of this Study

In this study, we scrutinize the chemo-mechanical coupling kinetics of the F_1-ATPase during the catalytic dwell at higher and lower temperature, where the single molecule observation cannot be done with the current technology. The chemo-mechanical coupling model of the catalytic dwell was first constructed by Watanabe et al. (2013)[21]. The number of the states (dwells) $N = 2$ so that P_i release takes place after hydrolysis successively. In addition, they introduced the angle-dependent rate constant $k_i(\theta) \propto e^{b_i\theta}$ based on the stall-and-release experiment with magnet tweezers,[11,20] where i represents hydrolysis or P_i release and b_i is a constant. Although the potential $U_i(\theta)$ is the same for the hydrolysis waiting state and the P_i release waiting sate in their setting, C.-B.Li et al.(2015)[17] modified it so that a $\sim 20^\circ$ angle shift takes place to manifest the small rotation after hydrolysis, making a clear distinction between the pre-hydrolysis dwell and the post-hydrolysis dwell. We adopted this model setting and expanded it so that we can change the temperature through the effective friction $\Gamma(T)$ and the angle-dependent rate constant $k_i(\theta;T)$ (explained in Sec.2.2.4).

The schematic picture and the mathematical description are as follows;

$$\begin{aligned}\frac{\partial P^{\rm pre}(\theta;t)}{\partial t} &= -\frac{\partial}{\partial\theta}\left\{-\frac{1}{\Gamma(T)}\frac{dU^{\rm pre}(\theta)}{d\theta}P^{\rm pre}(\theta;t)\right\} + \frac{k_BT}{\Gamma(T)}\frac{\partial^2}{\partial\theta^2}P^{\rm pre}(\theta;t) \\ &\quad - k_{\rm hyd}(\theta;T)P^{\rm pre}(\theta;t) + k_{\rm P_i}(\theta+120^\circ;T)P^{\rm post}(\theta+120^\circ;t),\end{aligned} \tag{2.4a}$$

$$\begin{aligned}\frac{\partial P^{\rm post}(\theta;t)}{\partial t} &= -\frac{\partial}{\partial\theta}\left\{-\frac{1}{\Gamma(T)}\frac{dU^{\rm post}(\theta)}{d\theta}P^{\rm post}(\theta;t)\right\} + \frac{k_BT}{\Gamma(T)}\frac{\partial^2}{\partial\theta^2}P^{\rm post}(\theta;t) \\ &\quad - k_{\rm P_i}(\theta;T)P^{\rm post}(\theta;t) + k_{\rm hyd}(\theta;T)P^{\rm pre}(\theta;t).\end{aligned} \tag{2.4b}$$

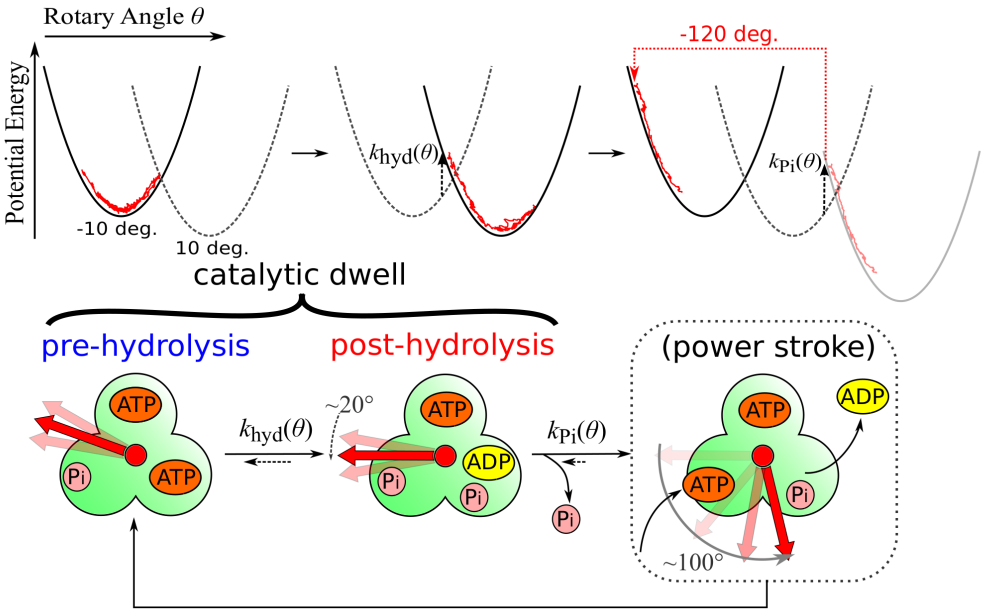

Fig.2.3: The schematic picture of the potential switching model (above) and and the F_1 kinetic scheme (below). The green shaped objects in the kinetic scheme picture show the F_1 molecule observed from above. The three circles show the catalytic sites of the $(\alpha\beta)_3$-subunit and the red arrow indicates the rotary angle of the γ-subunit.

$P^{\mathrm{pre/post}}(\theta;t)$ is the angle distribution in the pre- or post-hydrolysis dwell. The potential $U^{\mathrm{pre/post}}(\theta)$ is basically harmonic but smoothly connects to linear forms at left and right edges so that the torque $|dU^{\mathrm{pre/post}}(\theta)/d\theta|$ amounts to the experimental value at maximum (the detail is described later in this chapter).

$k_{\mathrm{hyd}}(\theta;T), k_{\mathrm{P_i}}(\theta;T)$ are the rate constants of hydrolysis and P_i release, respectively. In this setting, the backward reactions, i.e., ATP synthesis and P_i rebinding, are neglected because their rate constants are small enough compared with those of the forward reactions according to the result of the C.-B.Li et al.(2015).[17] We consider it a plausible approximation as long as we only look at the reaction timescales but from the view point of the energetics it is unreasonable because the zero rate constant means the activation free energy barrier height is infinite for backward reactions. If we scrutinize the energetics of this protein, we have to include the true values of the backward reaction rate constants after make it clear why the rate constant of the ATP synthesis appears to be zero during free rotation although non-negligible value is reported by the stall-and-release experiment.[20]

2.2.4 Temperature Dependence of the Model Setting

The temperature dependence is introduced to the angle-dependent rate constant $k_i(\theta;T)$ and the effective friction $\Gamma(T)$.

First, the angle-dependent rate constant is set as follows;

$$k_i(\theta) = \nu_i \exp\left(-\frac{\varepsilon_i - \alpha_i \theta}{k_B T}\right). \tag{2.5}$$

This is based on the interpretation that the result of the stall-and-release experiment $k_i(\theta) \propto e^{b_i \theta}$ [20] is due to the angle-dependent activation free energy. The activation free energy corresponds to $\varepsilon_i - \alpha_i \theta$, where ε_i is the averaged value over the rotary angle and the angle dependence coefficient α_i is related with the experimental result as $\alpha_i / k_B T = b_i$. The parameter ν_i is the prefactor and here it is constant. Theoretically it linearly depends on temperature T but that dependence is usually smaller than the exponential part and negligible. Moreover, we did not introduce θ dependence to this parameter for simplicity (discussed in detail in Sec.3.1.3).

Next, the temperature dependence of the effective friction constant $\Gamma(T)$ is set to be the same as that of pure water. Theoretically, the effective friction constant Γ of a sphere with radius a revolving around a fixed axis with revolution radius x_r is represented as below;[48,53]

$$\Gamma(T) = (8\pi a^3 + 6\pi a x_r^2)\eta(T), \tag{2.6}$$

where $\eta(T)$ is the solvent viscosity. Because we have no data on the temperature dependence of the solvent viscosity, we introduced an artificial assumption that it shows the same temperature dependence as pure water viscosity $\eta_{\mathrm{w}}(T)$, that is, $\eta(T) = C_\eta \eta_{\mathrm{w}}(T)$ with a proportionality constant C_η. This constant is determined from the data analysis results (shown later in this chapter).

2.2.5 Calculation with Langevin Representation

In the actual calculation, we used the Langevin equation instead of the Fokker-Planck representation in order to focus on the behavior of the single trajectory.

$$\Gamma(T)\frac{d\theta(t)}{dt} = -\frac{dU^{(\mathrm{pre/post})}(\theta)}{d\theta} + \sqrt{2\Gamma(T)k_B T}\,\xi(t) \tag{2.7a}$$

$$\langle \xi(t) \rangle = 0,\ \langle \xi(t_1)\xi(t_2) \rangle = \delta(t_1 - t_2), \tag{2.7b}$$

where $\xi(t)$ is a Gaussian white noise. The switching of the potential $U^{(\mathrm{pre/post})}(\theta)$ obeys the Poissonian process with the angle-dependent rate constant $k_i(\theta; T)$. The detail of the numerical calculation is in the Appendix A.2.

From the simulation trajectory of this Langevin equation, we calculate the dwell time distribution and the dwell time correlation. Although they could be calculated from the Fokker-Planck representation, the Langevin representation is easier.

2.3 Time Series Analysis I : Rotary Dwell Detection and Data Selection

The model discussed in the previous section included some parameters such as the effective friction $\Gamma(T)$, the prefactor and the averaged activation free energy of the angle-dependent rate constant (ν_i, ε_i). In order to make the model consistent with reality, we tune the model parameters based on the experimental data. The time series analysis for parameter tuning roughly consists of two parts; the first one

is the rotary dwell detection and the second one is the parameter inference. In this section, we explain the first one: the mathematical methods to select out rotary dwells from the noisy time series.

The aim of the methods is to objectively detect (catalytic) rotary dwell segments from the step-wise time series and determine which of the three catalytic dwells those segments belong to. The dwell segments detected in this way are used for dwell time analysis and calculating the physical quantities for the model parameter tuning (Sec.2.4). In order to do them, we apply two methods developed by C.-B. Li et al. (2015)[17] to the experimental data. The first one is the change point analysis (CPA) to detect at which time the trend of the time series drastically changed. The time series segment between the detected change points ideally corresponds to either a catalytic dwell or a rotation (power stroke) part. The second methods, the soft clustering based on information theory, assigns these segments into the rotation and one of the three catalytic dwells.

In addition to the CPA and the clustering, we also explain the dwell time analysis in this section because during this process we select out data sets we use throughout this research so that we can obtain reliable statistics.

2.3.1 Data Selection before Analysis

Before we apply time series analysis to the experimental data, we first selected out the data sets which do not contain obvious defects. By checking the rotary trace of each data, we excluded the ones which do not rotate in a clean circle and have too strong a deformation. Such data sets could be affected by destructive interaction with the glass surfaces where the molecule is attached or have defects in the molecular structure.

2.3.2 Change Point Analysis and Clustering Based on Information Theory

In order to distinguish at which time instant a rotary dwell or a rotation part begins and ends, we detect change points of the linear trend of the rotary angle time series. We first apply the least square linear fitting to the whole time series and decide whether there is at least one change point or not from the size of the fitting error. In order to subjectively quantify it, we calculate the difference time series from the linear trend and its cumulative sum adopting the difference between its minimum and maximum values as a criteria of the error. This quantity, denoted as D_{CUMSUM}, shows large value if the time series has some consistent trends because the time series largely deviates from the linear fitting line for longer time than the deviation due to the random fluctuation due to the thermal noises or shot noises. We permute the time ordering of the difference time series, where the consistent trends are destroyed, and construct the distribution of D_{CUMSUM} among many sets of the permuted time series. If D_{CUMSUM} of the original time series is larger than the 95% confident area of this distribution, we declare that there is at least one change point. Next, we locate the position of a change point. We divide the time series into two at an arbitrary time position and applied the linear least square fitting to both of the two segments. The change point is the dividing position where the sum of the least square errors for both segments is smallest. After that we repeated these procedures above to the two divided segments until no change

point is found and collect all the change points in the time series. We also estimate the uncertainties of the change point positions by the bootstrapping method[54] because the error in dwell lengths can affect the dwell time distribution, affecting the values of rate coefficients.

In order to assign the time series segments divided by these change points into the rotation part or one of the three (or six) rotary dwells, we apply a soft clustering method. This methods determines the conditional probability $P(C_\alpha|e_i)$ for a segment labeled as e_i to be assigned into a dwell labeled as C_α by an iteration algorithm to search for an optimized evaluation function based on the rate distortion theory in the information theory.[55] As an evaluation function, we adopt the sum of two quantities; the total sum of the angle difference among the change point segments assigned into the same cluster and the similarity between the change point segments before and after the clustering. The latter criteria corresponds to the data compressibility and is quantified by the mutual information.[55]

The details of these two methods are described in the supplemental information of C.-B. Li et al.(2015).[17]

2.3.3 Dwell Assignment

Based on the resulting conditional probability $P(C_\alpha|e_i)$, we assigned each time series segment into dwells and rotation. If the value of $P(C_\alpha|e_i)$ is higher than 0.95, we regarded that the ith segment belongs to the dwell labelled as α. When successive dwell segments are assigned to the same dwell, we remove the change point and connect them. This is due to the wrong detection of a change point, that is, the change point analysis detected a false change point although there is actually not (it is called false positive or type I error). This type of error often happens when an abrupt sharp noise appears during a dwell. On the other hand, if $P(C_\alpha|e_i)$ does not reach 95% for any α at certain i, we regard that this segment belongs to the rotation part or contains some detection error. An example of the error is as follows: a dwell is so short that the change point cannot be detected. In such cases one segment can contain more than two dwells and produce an intermediate value of $P(C_\alpha|e_i)$. In this study we only use the segments which are definitely assigned to one of the dwells because we focus on the dwell parts and do not investigate the rotation part.

The number of clusters N_C is the number of rotary dwells and it is fixed to $N_C = 3$ for $T \geq 20$. However, especially the temperature is not so high ($T = 16°$C), the ATP binding dwells are visible due to the temperature sensitive step so that we set $N_C = 6$.

2.3.4 Data Selection and Dwell Time Analysis

From the dwells detected and assigned by the CPA and clustering, we constructed dwell time survival distributions to obtain the rate coefficients of hydrolysis and $\mathrm{P_i}$ release. For the data at $T = 20, 25, 33°$C, the time series segments assigned as different catalytic dwells were treated separately as mentioned before. In addition, we also checked the number of segments in each dwell set and selected out the dwell sets with more than 100 segments. If the number of segments is less than 100, we did not use such dwell sets for further analysis because such data is so short that it could affect the statistics. For the data at $T = 16°$C,

however, no dwell set has more than 100 segments because the length of each segment is longer than other temperature on average. In order to construct reliable statistics for this temperature, we mixed some dwell sets if they satisfy the two conditions. First, these dwell sets are taken from the same molecule. Second, their dwell time distributions are statistically same based on the Kolmogorov-Smirnov test with 5% significance level.

After constructing the survival distribution, we checked its form in linear-log plotting. If its slope suddenly changes at much longer time region than ordinary hydrolysis or P_i release timescale, we discarded such dwell set because it could contain strange exponents due to some unknown factor.

Finally we fit the dwell time survival distributions of the selected dwell sets with exponential functions. In fitting the experimental data, we applied Padé-Laplace method [17,56,57]. This method calculates poles of the Laplace-transformed survival distribution with Padé approximation. The merit of this method is that it produces a fitting function based on the overall form of the data while the least square method ordinarily used puts weight according to the density of the data points so that it underestimates the effect of the part with small number of data points, that is, the tail part of the distribution with small probability. The number of the exponents is not assumed *a priori* but we find the appropriate number by truncating the terms with negligibly small coefficients.[*1] In most cases, however, we obtained two exponents as is expected from the conventional analysis and we regarded the larger one as the rate coefficient of P_i release and the smaller one as that of hydrolysis.

2.4 Time Series Analysis II : Parameter Inference

In the previous section, the rotary dwell was detected by the CPA and the clustering and dwell sets which can be used for further analysis were selected out. Based on these results, we tune the model parameters from the experimental time series. In the following, we discuss the details of the tuning method one by one.

2.4.1 Potential

The form of the potential is as follows;

$$U^{(\mathrm{pre/post})}(\theta) = \begin{cases} \frac{\kappa}{2}(\theta \pm \theta_d/2)^2 & |\theta \pm \theta_d/2| < \theta_T \\ T_\theta(\theta - \theta_T \pm \theta_d/2) + \frac{\kappa}{2}(\theta_T \pm \theta_d/2)^2 & \theta \pm \theta_d/2 > \theta_T \\ -T_\theta(\theta + \theta_T \pm \theta_d/2) + \frac{\kappa}{2}(\theta_T \pm \theta_d/2)^2 & \theta \pm \theta_d/2 < -\theta_T \end{cases} \tag{2.8}$$

θ_d is the angle displacement after hydrolysis and set to be 20° in this study. The bottom of the potential is at $\theta = \mp\theta_d/2$ for $-$: pre-hydrolysis dwell and $+$: post-hydrolysis dwell. The potential form is quadratic around the center with the spring constant κ. This is based on the experimental results that the rotary angle distribution $P(\theta_\gamma)$ in a catalytic dwell is Gaussian and the assumption of the Maxwell-Boltzmann distribution $P(\theta_\gamma) \propto \exp(-G(\theta_\gamma)/k_BT)$. However, the potential form is smoothly connected to a linear one at the outer regions $|\theta \pm \theta_d| > \theta_T = 43^\circ$. This modification follows the model in R. Watanabe et al.

[*1] More precisely, we defined area of each term as |(coefficient)/(exponent)| and truncated the terms whose area is smaller than 1% of the largest one.

2013[21] so that the torque $|dG(\theta)/d\theta|$ should not exceed the experimental value $T_\theta = 0.70$ pN nm deg.$^{-1}$ (= 40 pN nm rad.$^{-1}$).[2,58,59]

The value of the quadratic potential curvature $\kappa = 1.62 \times 10^{-2}$ pN nm deg.$^{-2}$ follows that of C.-B. Li et al. 2015[17], in which it was tuned so that the width of the rotary angle distribution in a catalytic dwell coincides with the experimental value. Although we have two potentials, pre and post-hydrolysis ones, in a catalytic dwell in our setting, they assumed that the experimentally observed rotary angle distribution is the overlap of the angle fluctuations in two sub-dwells and fixed the parameter κ to reproduce the experimental result by simulation. For simplicity, the curvatures of the two potentials are exactly the same. When the two potentials with the same curvatures are close together, the sum of the two Gaussian rotary angle fluctuations is also close to the Gaussian even if we take the population ratio in each of the sub-dwell into account.

2.4.2 Angle-Dependent Rate Constant

The switching rate of the potential (eqn.(2.5))

$$k_i(\theta) = \nu_i \exp\left(-\frac{\varepsilon_i - \alpha_i \theta}{k_B T}\right) \tag{2.9}$$

has three parameters; $\nu_i, \varepsilon_i, \alpha_i$. The angle-dependent parameter α_i is related with the experimentally observed coefficient b_i of the stall-and-release experiment $k_i(\theta) \propto e^{b_i \theta}$ as $\alpha_i / k_B T = b_i$. Because $b_{\mathrm{hyd}} = 0.019$ deg^{-1} and $b_{\mathrm{P_i}} = 0.12$ deg^{-1} at $T = 23°$C in the experiment[20], we set α_{hyd} and $\alpha_{\mathrm{P_i}}$ as in the Table 2.1 below.

ν_i and ε_i are determined at the same time combining the simulation and the experimental data. First of all, the angle-dependent rate constant can be rewritten as follows;

$$k_i(\theta) = A_i(T) e^{\alpha_i \theta / k_B T}, \tag{2.10a}$$

$$A_i(T) = \nu_i e^{-\varepsilon_i / k_B T}. \tag{2.10b}$$

We set arbitrary values of $A_i(T)$ to run the simulation and find appropriate ones to reproduce the experimental rate coefficients at 20, 25, 33°C obtained by the dwell time distribution fitting. Because there are many experimental data points for each temperature (different molecules, different sub-units), we used their average values. From the tuned values of $A_i(T)$ at each temperature, we obtained ν_i, ε_i by fitting with eq.(2.10b) (see Fig.2.4). The obtained values are listed in Table2.1.

Table2.1: Simulation parameters for angle-dependent rate constants

	α_i [pN·nm·deg.$^{-1}$]	ν_i [1/s]	ε_i [pN·nm] ([kJ/mol])
Hydrolysis	0.078	1.90×10^{12}	88.28 (53.16)
P_i release	0.47	1.18×10^{15}	121.8 (73.33)

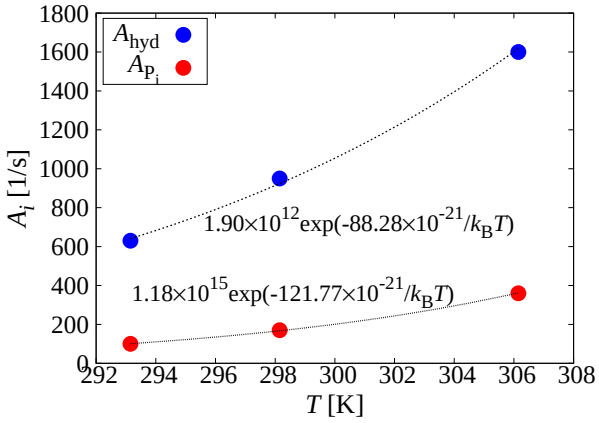

Fig.2.4: Fitting of the tuned values of the $A_i(T)$ with $\nu_i e^{-\varepsilon_i/k_BT}$ (eq.(2.10b)) at $T = 20, 25, 33°\mathrm{C}$.

2.4.3 Effective Friction Constant

The effective friction constant was obtained from the relaxation time of the rotary angle autocorrelation function $\langle\theta(0)\theta(t)\rangle$. For the simplest case, the equilibrium relaxation time of the Brownian particle coordinate in a harmonic potential is as follows;

$$\tau_{\mathrm{rel}} = \gamma/k. \tag{2.11}$$

This is obtained from an overdamped Langevin equation

$$\gamma\frac{dx(t)}{dt} = -kx(t) + \sqrt{2\gamma k_B T}\xi(t) \tag{2.12a}$$

$$\langle\xi(t)\rangle = 0,\ \langle\xi(0)\xi(t)\rangle = \delta(t), \tag{2.12b}$$

where the autocorrelation function of $x(t)$ is

$$\langle x(0)x(t)\rangle = \langle x(0)^2\rangle e^{-t/\tau_{\mathrm{rel}}}. \tag{2.13}$$

The detail calculation is in the Appendix A.1.2. On the other hand, the autocorrelation function of the rotary angle during the catalytic dwell is not single-exponential but double-exponential (see Fig.2.5). Because the result of the simulation with two quadratic potentials in a catalytic dwell also shows the double exponential autocorrelation decay, we assum that the first exponent with the shorter time constant (0.08[ms] at 25°C) is the local-equilibrium relaxation time in each of the two sub-dwells Γ/κ and that the second one with the longer time constant (0.48[ms] at 25°C), whose timescale is closer to the those of reactions (1.6[ms] for hydrolysis and 0.84[ms] for $\mathrm{P_i}$ release at 25°C) than the other's is, is due to the kinetic scheme with a small angle shift.

In this way, we obtained the effective friction constant Γ from the experimental time series for each of the molecules with different temperature. In order to run the extrapolative simulation at temperature higher or lower than that of the data sets we have, we have to introduce the temperature dependence into this parameter because it depends on the viscosity of the solvent. As mentioned in Sec. 2.2.4, we

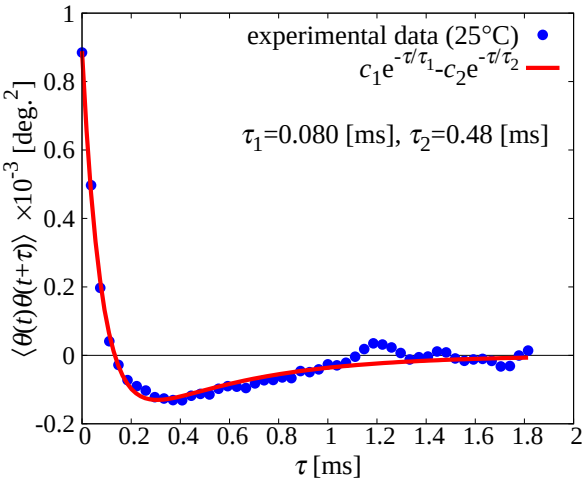

Fig.2.5: The autocorrelation function of the rotary angle during the catalytic dwell (experimental data, 25°C). Remark here that we subtracted the linear trend from the cumulative angle θ_γ for each catalytic dwell (denoted as $\hat{\theta}(t)$).

have to determine the proportionality constant C_η of $\eta(T) = C_\eta \eta_{\rm w}(T)$ under the assumption that the solvent viscosity shows the same temperature dependence as pure water. Using the theoretical relation (2.14)

$$\Gamma = (8\pi a^3 + 6\pi a x_r^2)\eta(T), \tag{2.14}$$

we estimated C_η from the data. a, the radius of the probe, gold nano-particle, is 40 nm. The revolution radius $x_{\rm r}$ is obtained from the rotary trace; we calculated the mean square of the distance between the coordinate of the probe and the revolution center for each molecule. Then we calculated the value of the constant for each data and obtained the averaged value $C_\eta = 3.0$ (see Fig.2.6(a)), which means the probe attached to the F_1 molecule feels the viscosity three times larger than that of pure water. From the view point of the hydrodynamical effect near the surface of the glass ($\sim$ 10nm),[60] this value is a reasonable one. In Fig.2.6(b), we showed the experimental values of the relaxation time and most of them are within the range of the theoretical values $\tau_{\rm rel} = \Gamma/\kappa$ with the revolution radius $x_{\rm r} = 0 \sim a$(=40nm). We consider it as a good approximation and used the value of Γ at the averaged revolution radius $x_{\rm r} = 24$nm in the simulation.

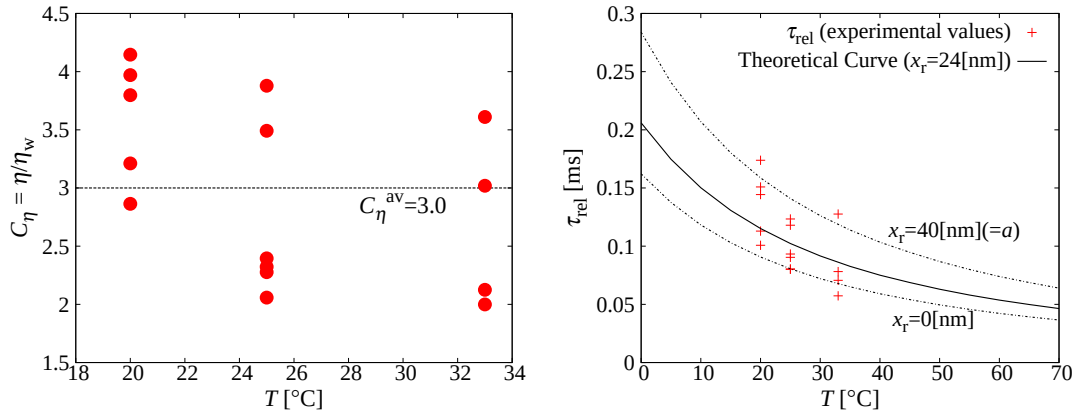

(a) (b)

Fig.2.6: (a) The ratio of the viscosity of the media against that of water for each time series. The values C_η are estimated from the relaxation time and eq.(2.14), using the revolution radii x_r measured from the rotary traces. (b) The relationship between temperature T and experimentally observed relaxation time τ_{rel} (red points) with theoretical curves using the average value of the proportionality constant $C_\eta^{av} = 3.0$. While the black curve shows the theoretical values with the average revolution radius $x_r = 24$ nm, the region within dash curves shows those of $x_r = 0 \sim 40$ nm (= bead radius a).

Chapter 3

Results and Discussion

Through the numerical simulation with the data-driven potential switching model discussed in the previous section, we obtained two results. The first one is the break of the Arrhenius relation at P_i release, which has been assumed in estimating the activation free energy. We also proposed a modified method to calculate the activation free energy and found positive entropy change at P_i release contrary to the original result. The next one is the emergence of the negative correlation between the hydrolysis and the P_i release waiting time in the same catalytic dwell. This correlation gets more conspicuous at temperature higher than 40°C and contributes to the deviation of the dwell time distribution from a double-exponential form at $T > 60$°C. Both of the results are caused by the onset of the non-equilibrium feature in the rotary angle fluctuation, induced by the competition between the reaction timescales and the diffusion timescale of the rotary angle in the reactive potentials.

3.1 Non-Arrhenius Relation Induced by Non-Equilibrium Angle Fluctuation

3.1.1 Arrhenius Plot of the Rate Coefficients

First, we looked at the temperature dependence of the rate coefficients of hydrolysis and P_i release at different temperature. Fig. 3.1 shows the Arrhenius plot, where $\log \bar{k}_i$'s are plotted as a function of $1/T$ so that a linear relationship appears when the Arrhenius law ($k_i(T) \propto \exp(-\Delta G_i^{\ddagger})$) holds. The solid blue and red lines are the simulation values for hydrolysis and P_i release rate coefficients, respectively. We also plotted experimental values by blue and red circles in order to show that the model is well tuned to reproduce real data within the range of temperature where the experiment was done. The remarkable feature of this plotting is that the simulated rate constant of P_i release slightly deviates from a straight line; as the temperature increases, its slope gets smaller. It suggests that the rate coefficients of the P_i release does not obey the Arrhenius law, which was assumed in R. Watanabe et al. (2014) [14] to estimate the activation free energy by linear fitting of the plot. On the other hand, the simulated rate coefficient of hydrolysis (blue solid line) shows a straight line and appears to obey the Arrhenius law.

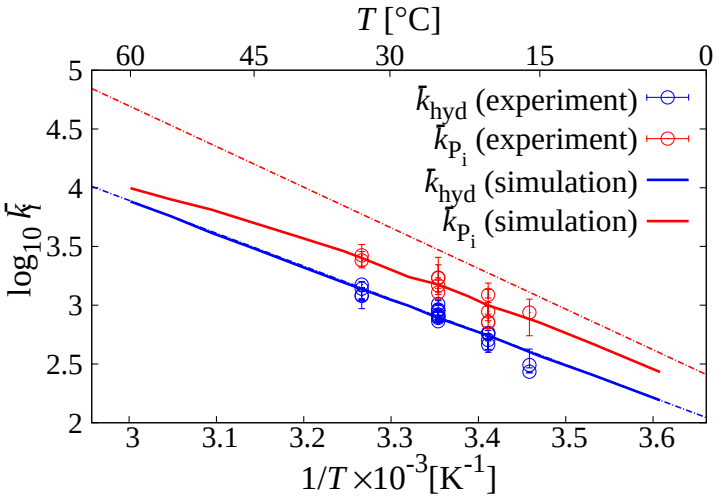

Fig.3.1: The Arrhenius plot of the rate coefficients of hydrolysis (blue) and P_i release (red).

3.1.2 Cause of the Non-Arrhenius Relation

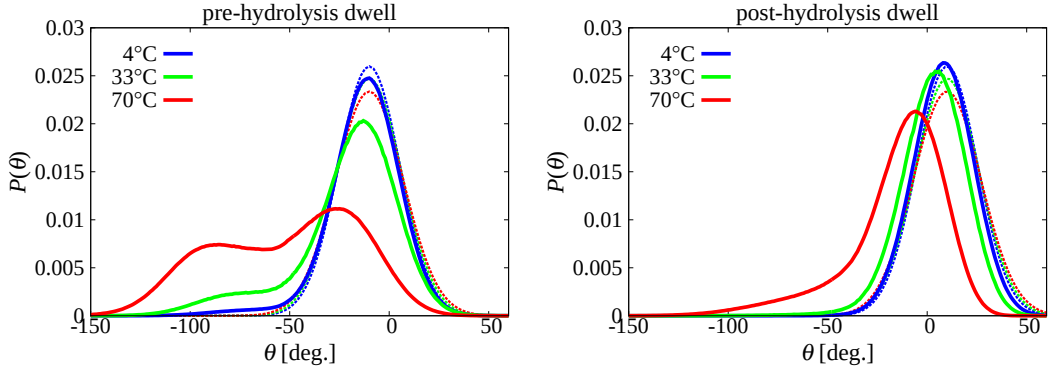

Fig.3.2: The steady state angle distribution at 4, 33, 70°C.

The reason of the breakdown of the Arrhenius law in P_i release is the deviation of the rotary angle fluctuation from the local-equilibrium one, localizing toward the region where the activation free energy is higher as temperature increases.

The solid lines in Fig. 3.2 show the steady state angle distribution during the pre-hydrolysis dwell (a) and the post-hydrolysis dwell (b) at three different temperature, 4°C (blue), 33°C (green), 70°C (red). The steady state angle distribution is the histogram of the rotary angle resided in each sub-dwell during one time series. As a reference, we also showed the local-equilibrium angle distributions with broken

curves, which were calculated from the Maxwell-Boltzmann distribution with the free energy potential of pre- and post-hydrolysis dwells, $P^{\rm eq}_{\rm pre/post}(\theta;T) \propto \exp(-G^{\rm pre/post}(\theta)/k_BT)$, under the assumption that the relaxation of the rotary angle (indirectly, the conformational relaxation of $(\alpha\beta)_3$-subunits) is always attained at every dwell before the corresponding reactions take place. We can find in both of the sub-dwells the steady state angle distributions shift toward the left side, the smaller angle region away from the local-equilibrium distribution, as the temperature increases.

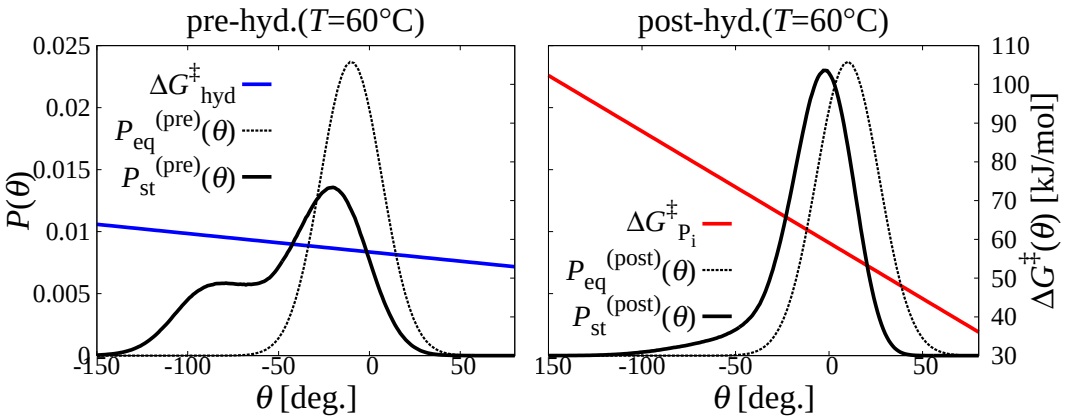

Fig.3.3: The steady state angle distributions in the pre- and post-hydrolysis dwells at 60°C ((a) and (b), respectively), with the activation free energy $\Delta G^{\ddagger}_{\rm hyd/P_i}(\theta)$.

On the other hand, the activation free energy is higher at the smaller angle region. In Fig. 3.3, we showed the steady state and local-equilibrium angle distributions at pre- and post-hydrolysis dwells at 60 °C ((a) and (b), respectively), with the Gibbs' activation free energy calculated from the angle dependent rate constants (eq.(2.5)) as $\Delta G^{\ddagger}_i(\theta) = -k_BT \log\{hk_i(\theta)/k_BT\}$ (blue and red solid lines, scales are the same for both figures). We can easily find that, the slope of the activation free energy along the rotary angle θ at the $\rm P_i$ release is much steeper than that at hydrolysis, which means that the rate coefficient of the $\rm P_i$ release is strongly affected by the rotary angle fluctuation; because the population of the rotary angle localizes towards the smaller angle region as the temperature increases, where the activation free energy barrier is higher than that in the local-equilibrium case. This rotary angle localization towards the less reactive region induces the non-Arrhenius temperature dependence in $\rm P_i$ release rate coefficients, while in hydrolysis the angle dependence of the static rate constant is so weak that the rate coefficient does not change so much even if the angle fluctuation largely deviates from the local-equilibrium in the pre-hydrolysis dwell.

The deviation from the quasi-equilibrium state can be explained by the competition of the two timescales mentioned above, the diffusion timescale vs the reaction timescales. As the temperature increases, both of the timescales get shorter as explained in Sec. 2.4; the diffusion constant through the lowering of the media viscosity (see eq.(2.5)), the reaction timescales through the Arrhenius law assumed for the angle-dependent rate constants (see eq.(2.14)). However, the reaction timescales get even shorter

than that of diffusion. For this reason, the rotary angle relaxation cannot catch up with the potential switching as the temperature increases, which leads to the larger deviation from the local-equilibrium distribution, that is, the non-equilibrium state.

In order to signify this non-equilibrium effect, we also showed the hypothetical fast diffusion limit (FDL) lines in the Arrhenius plot (Fig. 3.1, broken lines), where the local-equilibrium is assumed to hold always in each dwell as represented by

$$\begin{aligned} \bar{k}_i^{\mathrm{FDL}}(T) &= \int k_i(\theta;T) P^{\mathrm{eq.}}_{\mathrm{pre/post}}(\theta;T) d\theta \\ &= \nu_i \exp\left\{ -\frac{1}{k_B T}\left(\varepsilon_i - \frac{\alpha_i^2}{2\kappa} \right) \right\}. \end{aligned} \tag{3.1}$$

While the simulation line of the hydrolysis almost coincides with the FDL line, the $\mathrm{P_i}$ release simulation value shows larger deviation from FDL as the temperature increases. This shows that the $\mathrm{P_i}$ release rate coefficient is significantly suppressed by the retarded relaxation of the rotary angle fluctuation. In

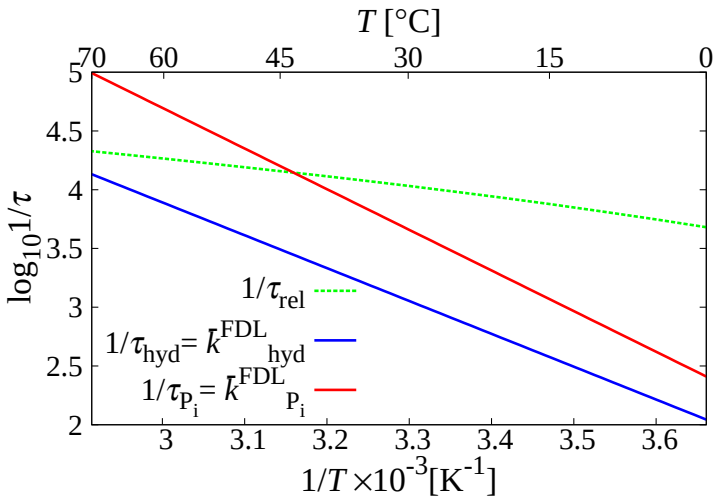

Fig.3.4: The comparison of the reaction timescales and the diffusion timescale, which are represented by $1/\bar{k}_i^{\mathrm{FDL}}$ and τ_{rel}, respectively.

addition, we visualized the competition of the diffusion timescale and reaction timescales in a quantified way in Fig. 3.4, where the reaction timescales are represented by the inverse of the FDL rate constants $1/\bar{k}_i^{\mathrm{FDL}}$ and the diffusion timescale by the relaxation time constant τ_{rel} of the angle autocorrelation function $\langle \theta(0)\theta(t) \rangle \propto e^{-t/\tau_{\mathrm{rel}}}$ (see more details in the Appendix). We can find that both of the timescales get the close values as the temperature increases. Especially for $\mathrm{P_i}$ release, the reaction timescale even exceeds the diffusion timescale.

Meanwhile, the deviation of the steady state angle distribution from the local-equilibrium one is larger for hydrolysis than $\mathrm{P_i}$ release. This is explained by the size of the angle shift after the potential switching and the angle dependence of the rate constants. While the equilibrium position of the potential shifts only 20° after the hydrolysis, there is a 100° shift after $\mathrm{P_i}$ release before landing on the following pre-hydrolysis

dwell to reach its equilibrium position. Moreover, due to the weak angle dependence of the hydrolysis rate constant, the probability to land onto the next post-hydrolysis dwell is almost independent of the rotary angle, which means that the switching can easily happen even during the rolling down toward the equilibrium position of the pre-hydrolysis dwell. On the other hand in the post-hydrolysis dwell, there is only 20° shift after the hydrolysis and the rate constant of P_i release is so sensitive to the angle that the angle where the reaction happens is almost limited to the large angle region. To make this mechanism simple, we can roughly say that the reaction window is narrower in P_i release than hydrolysis. In Fig. 3.5,

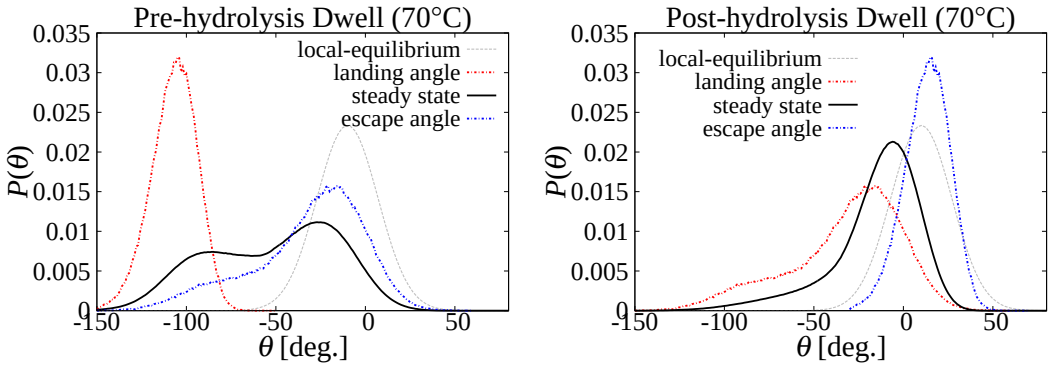

(a) (b)

Fig.3.5: Three types of the rotary angle distributions for pre- and post-hydrolysis dwells ((a) and (b), respectively) at 70°C; the landing angle distribution, the escape angle distribution, and the steady state angle distribution (black solid curve). The local-equilibrium angle distribution is also shown (grey curve).

we showed the three types of the rotary angle distributions for the pre- and post-hydrolysis dwells; the steady state angle distribution, the landing angle distribution, and the escape angle distribution. The landing angle is where a pre- or post-hydrolysis dwell begins, that is, the initial angle of the dwell. The escape angle is the angle where the reaction happens and the system moves onto the next sub-dwell. The escape angle distribution is sharper at P_i release although the landing angle distribution is wider. This escape angle distribution width corresponds to the reaction window.

Here we have to remark one thing about the steady state angle distribution. We can find that the steady state angle distribution of the pre-hydrolysis dwell has two peaks at higher temperature especially around $60 \sim 70$°C. However, the second peak, the left one, is only the artifact due to the potential cut-off. As explained in Sec. 2.4, the potential form is not exactly quadratic, we introduced linear slope at the edges ($|\theta - \theta_c| > 43.1°$) so that the torque produced in the potential should not exceed the experimental value. Especially at the pre-hydrolysis dwell, this cut-off exists in $\theta < -53.1°$, close to the region where the system leaves the previous post-hydrolysis dwell and new pre-hydrolysis dwell begins (Fig. 3.6(a), red broken curve). Because of this modification, the velocity of the rotation gets slower than would be at the quadratic form around $\theta = -100 \sim -50°$ and the rotary angle distribution is more likely to localize around there. In order to show this, we compared the steady state angle distributions between the two types of the potentials in Fig. 3.6; the ones with and without the straight cut-off (red and blue

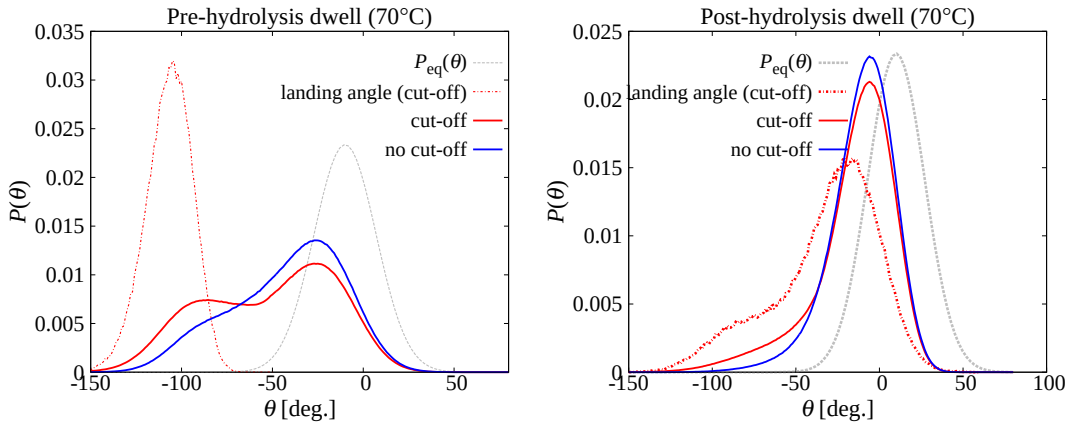

(a) (b)

Fig.3.6: The comparison of the two types of potentials. While the red solid curves were obtained with quadratic potentials with the straight cut-off at the edges, the same model as other results in this work, the blue solid curves were obtained with simple quadratic potentials. The landing angle distributions and the local-equilibrium angle distributions (grey broken curves) are also shown.

solid lines, respectively). The steady state angle distribution with simple quadratic potentials does not show the second peak although still there is small shoulder, which is the reminiscent of the landing angle distribution, the initial distribution, of the pre-hydrolysis dwell.

3.1.3 Correction of the Activation Free Energy for Non-Arrhenius Case

We showed that the Arrhenius law does not always hold for the "rate constants" obtained from the dwell analysis. In some experimental works[14,49], however, the activation free energy is often obtained from the linear fitting of the Arrhenius plot. Because this way of estimation may lead to erroneous values, we propose the modification in analysis using the experimentally tuned angle dependent rate constants (2.5), static values, instead of the direct use of the rate coefficients.

First of all, in the original experimental work[14], the activation Gibbs' free energy $\Delta G_i^{\ddagger}$, its entropy contribution $T\Delta S_i^{\ddagger}$, and the activation enthalpy $\Delta H_i^{\ddagger}$ were calculated from the Arrhenius plot, using the thermodynamic relation

$$\Delta G_i^{\ddagger} = \Delta H_i^{\ddagger} - T\Delta S_i^{\ddagger}. \tag{3.2}$$

This relation holds when the temperature is constant before and during the reaction ($\Delta T = 0$). While $\Delta G_i^{\ddagger}$ was calculated from the transition state theory $\bar{k}_i = \frac{k_B T}{h} \exp(-\Delta G_i^{\ddagger}/k_B T)$, $\Delta H_i^{\ddagger}$ and $T\Delta S_i^{\ddagger}$ were obtained from the slope and y-intercept at $1/T \to 0$ of the Arrhenius plot of $\bar{k}_i$. The problem of this calculation is that the temperature dependence of the rate coefficient $\bar{k}_i$ originates not only from the activation enthalpy $\Delta H_i^{\ddagger}$ but also from the the rotary angle fluctuation, which is also temperature dependent. We removed this dynamical effect due to the competition of the reaction and diffusion timescales by looking at the angle-dependent rate constant $k_i(\theta)$, to which we assumed the transition

state theory can be applied as

$$
\begin{aligned}
k_i(\theta;T) &= \frac{k_BT}{h}\exp\left(-\frac{\Delta G_i^{\ddagger}(\theta)}{k_BT}\right) \\
&= \frac{k_BT}{h}\exp\left(\frac{\Delta S_i^{\ddagger}}{k_B}\right)\exp\left(-\frac{\Delta H_i^{\ddagger}(\theta)}{k_BT}\right).
\end{aligned}
\tag{3.3}
$$

Here we used the thermodynamic relation (3.2) again. Although the entropy contribution $\Delta S_i^{\ddagger}$ also depends on the angle in general consideration, here we neglect this dependence (explained later in detail). Under this assumption, the angle dependent thermodynamic quantities are represented as below;

$$\Delta G_i^{\ddagger}(\theta) = -k_BT\log\left(\frac{hk_i(\theta)}{k_BT}\right) \tag{3.4a}$$

$$\Delta H_i^{\ddagger}(\theta) = \varepsilon_i - \alpha_i\theta \tag{3.4b}$$

$$T\Delta S_i^{\ddagger} = k_BT\log\left(\frac{h\nu_i}{k_BT}\right) \tag{3.4c}$$

Using these new relations, we showed the modified activation free energy values and compared the new values with those in the previous result in Fig.3.7 and Table 3.1. For the sake of the comparison, we

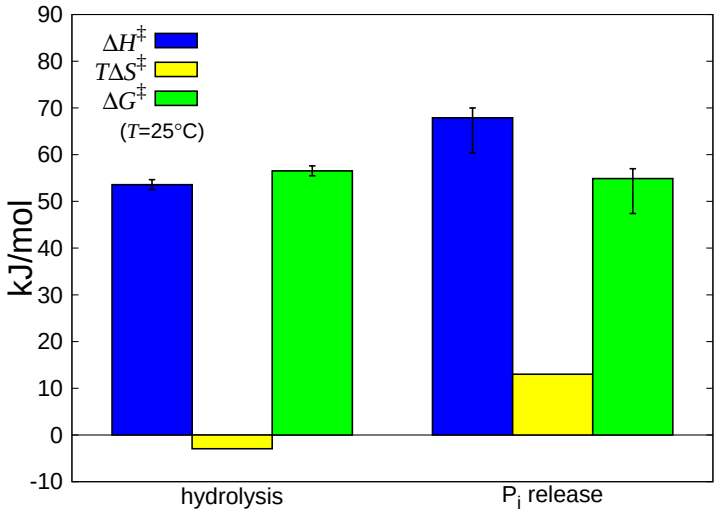

Fig.3.7: The modified values of the activation free energy of the hydrolysis and P_i release, taking the non-equilibrium effect into account.

calculated the represented values of the activation Gibbs' free energy in the same way as the original paper, $\Delta G_i^{\ddagger} = -k_BT\log\left(\frac{h\bar{k}_i}{k_BT}\right)$, while $\Delta S_i^{\ddagger}$ was directly calculated from eq.(3.4c). The activation enthalpy term was calculated from the thermodynamic relation (3.2) as $\Delta H_i^{\ddagger} = \Delta G_i^{\ddagger} - T\Delta S_i^{\ddagger}$. These $\Delta G_i^{\ddagger}$ and $\Delta H_i^{\ddagger}$, angle independent values, roughly correspond to the averaged values over the angle fluctuation, although they cannot be directly equated with the angle dependent ones as $\int \Delta G_i^{\ddagger}(\theta)P_{\mathrm{pre/post}}(\theta)d\theta$. In order to visualize how these quantities vary with the angle fluctuation, we showed with error bars the

Table3.1: Comparison of thermodynamic quantities for reactions at 25°C

units: [kJ/mol]		$\Delta G_i^{\ddagger}$	$\Delta H_i^{\ddagger}$	$T\Delta S_i^{\ddagger}$
Watanabe et al. 2014[14]	Hydrolysis	56	51	-5.4
	P_i release	53	39	-14
Non-Arrhenius modification	Hydrolysis	57	54	-2.9
	P_i release	55	68	13

values of the angle dependent values $\Delta G_i^{\ddagger}(\theta), \Delta H_i^{\ddagger}(\theta)$ within the 10%∼90% range of the rotary angle distribution.

Comparing the new values with the previous results (Table 3.1), we can find that the activation enthalpy $\Delta H_{\mathrm{P_i}}^{\ddagger}$ gets larger and that the entropy contribution term $T\Delta S_{\mathrm{P_i}}^{\ddagger}$ is modified into positive in the P_i release while there is no qualitative difference in those of the hydrolysis. In general, the activation entropy $\Delta S_i^{\dagger}$ is related to the prefactor (see eq. (3.4c)) and corresponds to the difference of the reactive potential widths between the reactant state and the transition state, roughly speaking the mobility difference of the reacting molecules. While the catalytic interface of the $(\alpha\beta)_3$-subunit opens so that the entropy is considered to increase at P_i release, the negative value of $\Delta S^{\ddagger}$ in P_i release came out in the original paper and they ascribed it to the loss of the water entropy surrounding the catalytic interface by excluding the volume for water molecules.[61] On the contrary, our modified result can be explained only by the conformational entropy gain without taking the water molecule effect into account.

In this work, we did not include the angle dependence in the activation entropy $\Delta S_i^{\ddagger}$ as mentioned above. It is natural to consider that this quantity also depends on the rotary angle because the mobility of the reacting molecule can be changed with the opening and closing motion of the catalytic interface along with the γ-subunit rotation. However, it is quite difficult to detect the angle dependence of both $\Delta S_i^{\ddagger}$ and $\Delta H_i^{\ddagger}$ at the same time and this is why we introduced an artificial assumption that only the enthalpy term has the angle dependence. If both $\Delta S^{\ddagger}(\theta)$ and $\Delta H^{\ddagger}(\theta)$ have the angle dependence, the angle dependence parameter b of the static rate constant $k_i(\theta) \propto e^{b\theta}$ can be expressed as below;

$$b = \frac{d \log k_i(\theta)}{d\theta} = \frac{1}{k_B}\frac{d\Delta S_i^{\ddagger}(\theta)}{d\theta} - \frac{1}{k_B T}\frac{d\Delta H_i^{\ddagger}(\theta)}{d\theta}. \tag{3.5}$$

This suggests that we can separate the angle dependence of these two thermodynamic quantities from the temperature dependence of the parameter b, which can be theoretically studied by the stall-and-release experiments at different temperature. Actually, similar measurement is already done at the ATP binding dwell for the ATP binding and the temperature sensitive steps[62] but the precision is not good enough so far. We consider that revealing the detailed angle dependence of the activation thermodynamic will provide the key to understand the dominant cause of the reactions, for example, the mechanical conformational change or the change in the electronic charge distribution.

3.2 Negative Correlation between Hydrolysis and P_i Release Waiting Time

3.2.1 Negative Correlation

The second thing we looked at is the correlation between the waiting time for the successive chemical reactions.

As the indicator of the correlation, we consider the Pearson's linear correlation coefficient. Given the probability density distribution of the pre- or post-hydrolysis dwell time as $P(\tau_i)$ and their joint probability as $P(\tau_i, \tau_j)$, the correlation coefficient $C_{i,j}$ is defined as

$$C_{i,j} = \frac{\sigma_{i,j}}{\sigma_i \sigma_j}, \tag{3.6}$$

where the covariance $\sigma_{i,j}$ and the standard deviation σ_i is defined by using the average $\langle \tau_i \rangle$ as

$$\langle \tau_i \rangle = \int_0^\infty \tau_i P(\tau_i) d\tau_i \tag{3.7a}$$

$$\sigma_i = \left(\int_0^\infty (\tau_i - \langle \tau_i \rangle)^2 P(\tau_i) d\tau_i \right)^{1/2} \tag{3.7b}$$

$$\sigma_{i,j} = \int_0^\infty \int_0^\infty (\tau_i - \langle \tau_i \rangle)(\tau_j - \langle \tau_j \rangle) P(\tau_i, \tau_j) d\tau_i d\tau_j. \tag{3.7c}$$

The indices i, j show which of the sub-dwells, pre-hydrolysis or post-hydrolysis dwell. The quantity $C_{i,j}$ takes the value between $[-1, 1]$ and equals to 0 when τ_i and τ_j are independent, that is, $P(\tau_i, \tau_j) = P(\tau_i)P(\tau_j)$. In order to calculate this value from the finite number of the sub-dwell time samples $\{\tau_i^{(k)}\}$, $k = 1, 2, ..., N$, where $\tau_i^{(k)}$ is the pre- or post-hydrolysis dwell time of the kth catalytic dwell, we used the discretized quantities below;

$$\langle \tau_i \rangle = \frac{1}{N} \sum_k \tau_i^{(k)} \tag{3.8a}$$

$$C_{i,j} = \frac{\frac{1}{N-1} \sum_k^N (\tau_i^{(k)} - \langle \tau_i \rangle)(\tau_j^{(k)} - \langle \tau_j \rangle)}{\sqrt{\frac{1}{N-1} \sum_k^N (\tau_i^{(k)} - \langle \tau_i \rangle)^2} \sqrt{\frac{1}{N-1} \sum_k^N (\tau_j^{(k)} - \langle \tau_j \rangle)^2}}. \tag{3.8b}$$

We calculated the correlation coefficients (3.8*b*) for two types of successive sub-dwell pairs. The first one is for the pre-hydrolysis dwell time and the post-hydrolysis dwell time in the same catalytic dwell $\{\tau_{\rm pre}^{(k)}, \tau_{\rm post}^{(k)}\}$. The next one is for the POST-hydrolysis dwell time and the NEXT pre-hydrolysis dwell time, denoted as $\{\tau_{\rm post}^{(k)}, \tau_{\rm pre'}^{(k)}\}$, where $\tau_{\rm pre'}^{(k)} = \tau_{\rm pre}^{(k+1)}$. The difference from the first one is that these sub-dwells are in different catalytic dwells separated by the 120° rotation.

In Fig. 3.8, we showed $C_{\rm pre,post}$ (blue) and $C_{\rm post,pre'}$ (red) at different temperature ($4 \sim 70$°C). While $C_{\rm post,pre'}$ is almost 0 for all of the temperature in the simulation, $C_{\rm pre,post}$ gets more negative as the temperature increases. The negative value of the correlation coefficient suggests that the two values, pre- and post-hydrolysis dwell time in the same catalytic dwell $\{\tau_{\rm pre}^{(k)}, \tau_{\rm post}^{(k)}\}$, cannot get longer or shorter than certain values at the same time; when the hydrolysis takes much longer time than the average, it is more likely that the next P_i release takes much shorter time than the average, and vise versa.

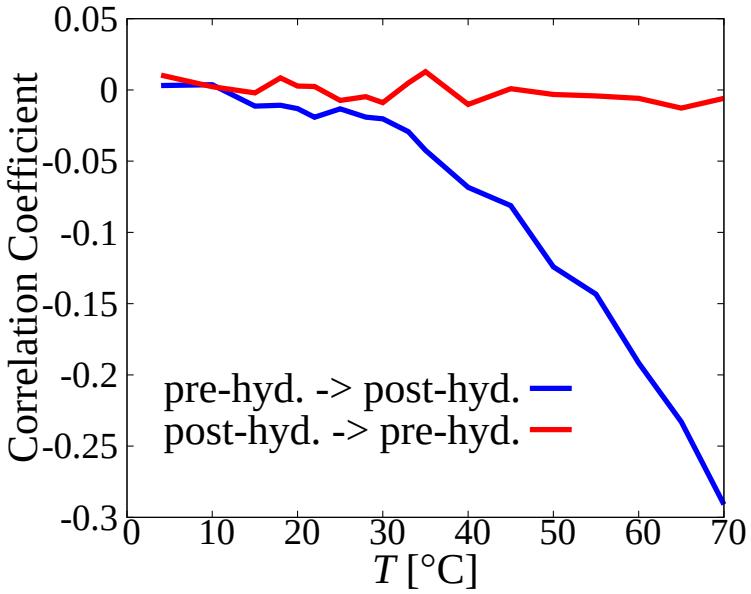

Fig.3.8: The correlation coefficients between the pre- and post-hydrolysis dwell time (T = 4 $\sim$ 70°C).

In order to show this, we also show the 2D plot for the two-body correlation $C(\tau_{\rm pre}, \tau_{\rm post}) = P(\tau_{\rm pre}, \tau_{\rm post}) - P(\tau_{\rm pre})P(\tau_{\rm post})$ at 4, 33, 70°C in Fig. 3.9. The positive (negative) value of $C(\tau_{\rm pre}, \tau_{\rm post})$, the red (blue) region in the figure, means the event of $\{\tau_{\rm pre}^{(k)}, \tau_{\rm post}^{(k)}\}$ pair is more (less) likely to occur than would if the two values were independent each other. Although there is no consistent structure in the $C(\tau_{\rm pre}, \tau_{\rm post})$ map at 4°C (Fig. 3.9(a)), a clearer contrast of the positive and negative region appears as the temperature increases. At 70°C (Fig. 3.9(c)), we can find that the occurrence of $\{\tau_{\rm pre}^{(k)}, \tau_{\rm post}^{(k)}\}$ pair with both $\tau_{\rm pre}$ and $\tau_{\rm post}$ shorter than 0.05 ms (blue region) is much less likely than the hypothetical independent case. On the other hand, $\tau_{\rm post}$ longer than 0.1 ms is more likely to appear after $\tau_{\rm pre}$ shorter than 0.1 ms, the same thing is true for $\tau_{\rm post} > 0.1$ ms after $\tau_{\rm pre} < 0.1$ ms (red region). For comparison, we remark that the reaction time constants of the hydrolysis at the fast diffusion limit $(1/\bar{k}_{\rm hyd}^{\rm FDL})$, regarded as the standard reaction timescale, is about 7.4×10^{-2} ms at 70°C, which is just between 0.05$\sim$0.1 ms, and comparing it with the case at 33°C (Fig. 3.9(b)), the negative correlation region (blue area) can be regarded as getting larger.

On the other hand, the two-body correlation between the post-hydrolysis dwell time and its successive pre-hydrolysis dwell time $C(\tau_{\rm post}, \tau_{\rm pre'})$ has no consistent pattern at 4, 33, 70°C (Fig. 3.10), which is consistent with the almost zero correlation coefficient (Fig. 3.8 red line). This result suggests that the memory of the catalytic dwell time is almost completely erased during the 120°C rotation and that we can regard each catalytic dwell time as independent.

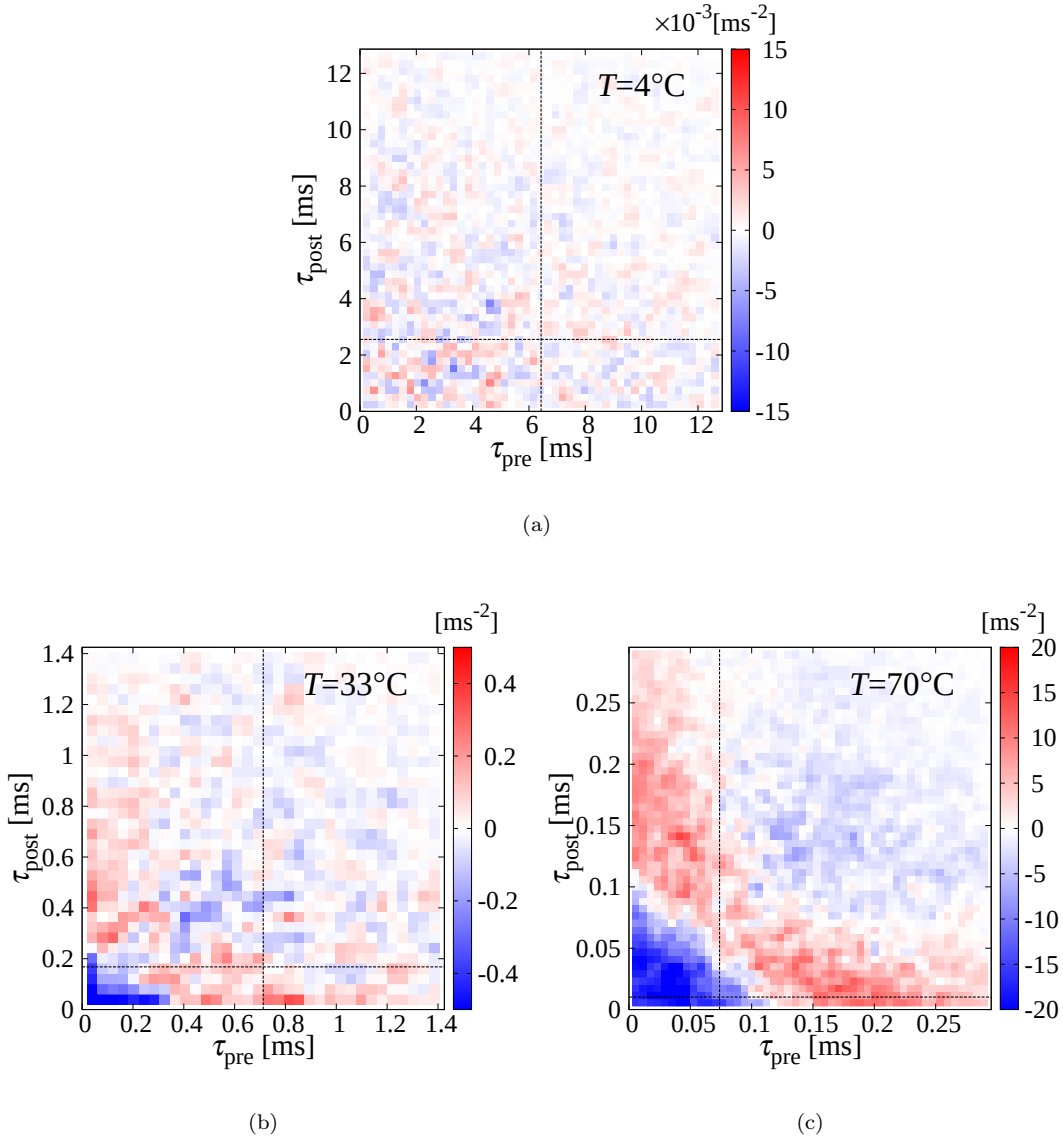

Fig.3.9: The 2D graphs of the two-body correlation $C(\tau_{\rm pre}, \tau_{\rm post})$ for the pre- and post-hydrolysis dwell time in the same catalytic dwell. The two crossing broken lines are shown to indicate the standard hydrolysis and P_i release timescales, $\bar{\tau}_{\rm hyd} = 1/\bar{k}^{\rm FDL}_{\rm hyd}$ and $\bar{\tau}_{P_i} = 1/\bar{k}^{\rm FDL}_{P_i}$, respectively.

3.2.2 Mechanism

The negative correlation between the pre- and post-hydrolysis dwell time in the same catalytic dwell is also induced by the angle dependent rate constant and the non-equilibrium feature. Because of the strong angle dependence of the P_i release rate constant, the dwell time in a post-hydrolysis potential is sensitive to the initial angle, at which the hydrolysis takes place and the system lands onto the post-hydrolysis potential. As the P_i release reaction is easier to take place at larger angle region (around $\theta > 10°$,

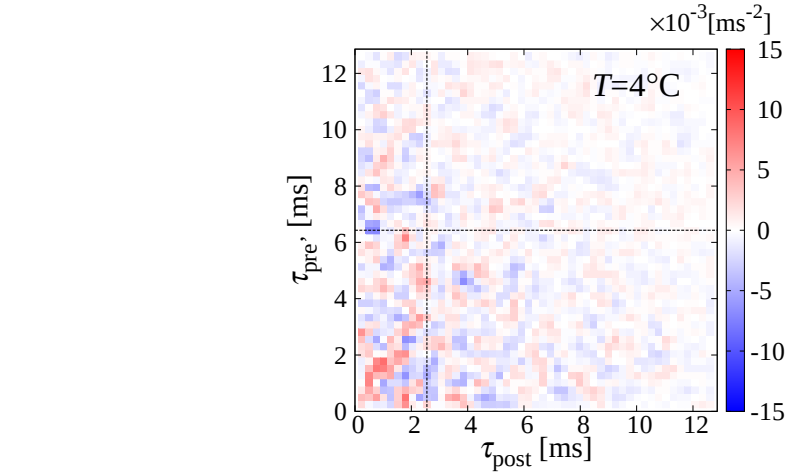

(a)

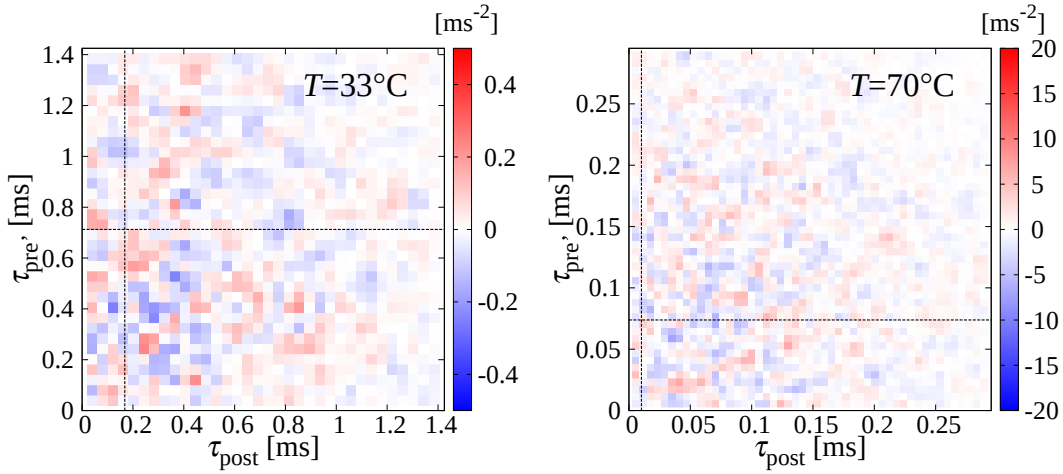

(b) (c)

Fig.3.10: The 2D graphs of the two-body correlation $C(\tau_{\rm post}, \tau_{\rm pre'})$ for the post-hydrolysis dwell time and the next pre-hydrolysis dwell time in the different catalytic dwells. The crossing broken lines indicates the standard timescale of P_i release and hydrolysis (the same as Fig. 3.9).

roughly regarded as the reaction window, see Fig. 3.5), the closer the landing angle is to this region, the shorter it takes to escape from the post-hydrolysis dwell. When the pre-hydrolysis dwell time is long enough for θ to reach larger angle region, then the system is likely to jump onto the post-hydrolysis potential at θ close to the reaction window. When the pre-hydrolysis dwell time is too short, however, this means that the hydrolysis reaction takes place at the smaller angle region (around $\theta < -50°$), from which the γ-subunit must take some time to rotate and reach the reaction window, releasing the P_i. When the diffusion timescale is much shorter than the reaction timescales, this does not happen because

the γ-subunit rotates quick enough to reach the reaction window so that the landing angle dependence of the dwell time is negligible. However, as the reaction timescales get shorter and surpasses the diffusion timescale with the increasing temperature, the weight of the diffusion time to approach the reaction window becomes larger in the post-hydrolysis dwell time, producing larger dependence on the landing angle. At the same time, the landing angle distribution itself shifts toward the smaller angle region, farther from the reaction window, as the rotary angle fluctuation in the pre-hydrolysis dwell deviates from the local-equilibrium one (Fig. 3.2). This is how the negative correlation is produced and enhanced as the temperature increases.

On the other hand, the almost zero correlation between the post-hydrolysis dwell time and the pre-hydrolysis dwell time in the successive different catalytic dwells is explained relatively easily. Because the angle dependence of the hydrolysis rate constant is much weaker than the P_i release, the dwell time in a pre-hydrolysis potential is not affected by the initial condition, at which angle the P_i is released and the system lands onto the pre-hydrolysis potential. This is why the two dwell times are not correlated no matter how far the system is from the quasi-equilibrium state as a result of the increasing temperature.

3.2.3 The Contribution to the Deformation of the Dwell Time Distribution

The negative correlation between pre- and post-hydrolysis dwell time in the same catalytic dwell is one of the causes to deform the dwell time distribution from a double-exponential function and make it unable to obtain the rate coefficients.

There are three assumptions in using the double-exponential function, $P(\tau) = c\{\exp(-k_{\mathrm{hyd}}\tau) - \exp(-k_{P_i}\tau)\}$ with a constant c, to fit the (catalytic) dwell time distribution and obtain the rate constants of the hydrolysis and P_i release;

1. The two reactions are successive.
2. The waiting time of each of the reactions obeys the single-exponential distribution.
3. The waiting time of the two reactions are independent.

As to the first one, the reaction order of the hydrolysis and P_i release in a catalytic dwell is experimentally reported that the hydrolysis is the first.[11,17] The validation of the second and third ones are not reported for F_1-ATPase, but usually they are considered to hold. However, as to the second one, the multi-exponential distribution of catalytic turnover time is often discussed from the viewpoint of the dynamic disorder[39] both theoretically[43,44,46] and experimentally[40,42]. Actually in our calculation, the distributions of the pre- and post-hydrolysis dwell time are separately obtained and both found to deviate from single exponential forms at temperature higher than 60°C (Fig. 3.11). This is due to the multiple reaction pathways caused by the non-equilibrium rotary angle fluctuation. At the same time, our result of the negative correlation shows that the third assumption, the independence of the successive reactions, can also be violated at high temperature. Actually, we consider this contributes to the deformation of the dwell time distribution.

As explained in 3.2.1, the negative correlation means that the hydrolysis and P_i release waiting time cannot be shorter than certain length at the same time. This suggests that the population of the short

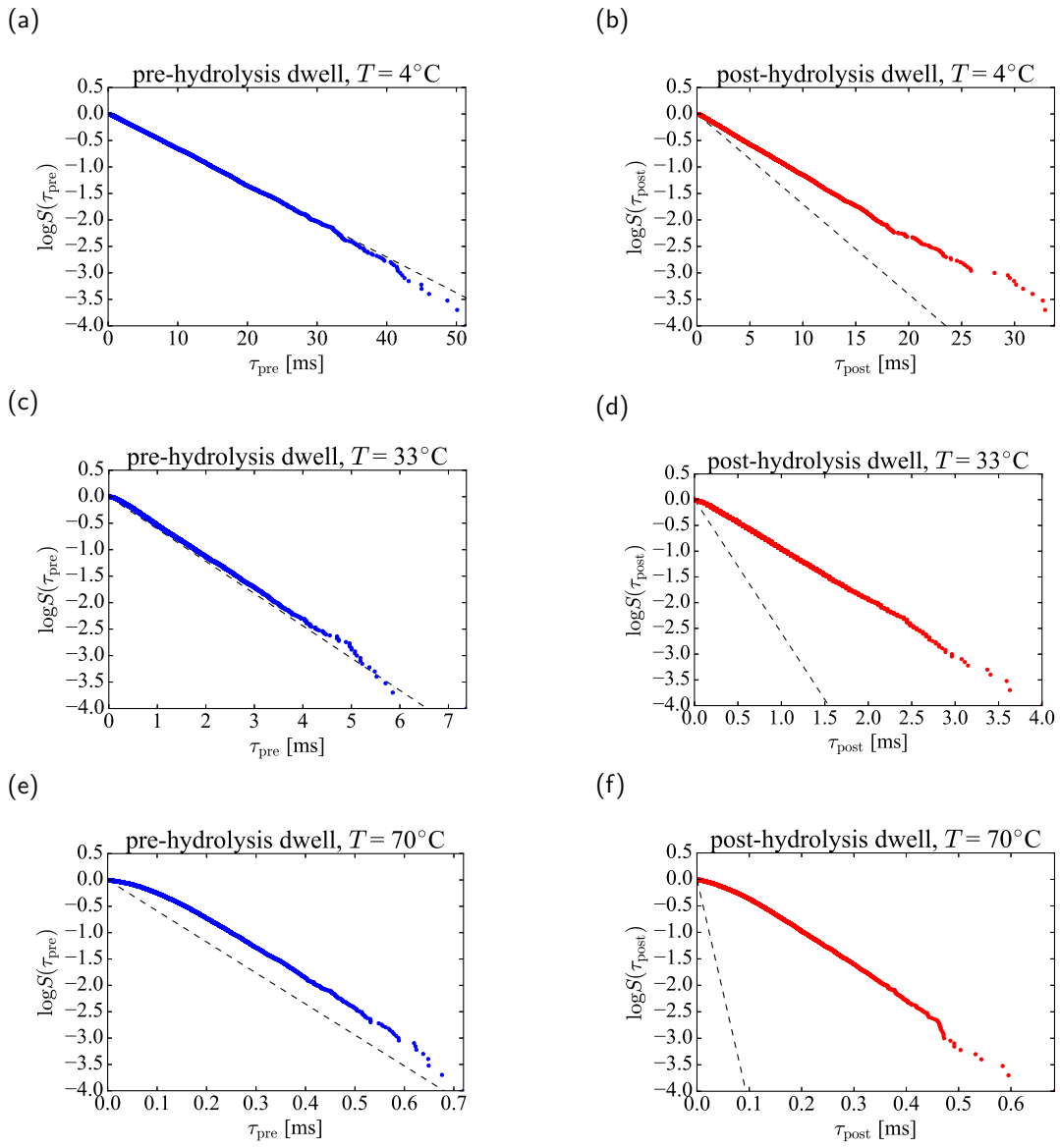

Fig.3.11: The survival distributions of sub-dwell time; pre-hydrolysis dwell time (left column) and post-hydrolysis dwell time (right column) at T =4°C (first row), 33°C (second row), and 70°C (third row). The broken lines show the single exponential functions with fast diffusion limit rate constants $\bar{k}_i^{\mathrm{FDL}}$.

catalytic dwell time (the sum of the pre- and post-hydrolysis dwell time $\tau = \tau_{\mathrm{pre}} + \tau_{\mathrm{post}}$) can be smaller than that in the situation when the two reactions are independent. In Fig. 3.12, we showed the simulation result of the dwell time survival distribution at 4, 33, 70°C. The grey curves are the theoretical values of the survival distribution $S(\tau) = \frac{k_1 k_2}{k_2 - k_1}\{\exp(-k_1\tau)/k_1 - \exp(-k_2\tau)/k_2)\}$ assuming the fast diffusion limit for both hydrolysis and $\mathrm{P_i}$ release, $k_1 = \bar{k}_{\mathrm{hyd}}^{\mathrm{FDL}}$, $k_2 = \bar{k}_{\mathrm{P_i}}^{\mathrm{FDL}}$, as a guide to show how the dwell time distribution deforms due to the non-equilibrium effect. At low temperature, 4°C (Fig. 3.12(a)), the deviation from the hypothetical fast diffusion limit curve is not so evident. However, as the temperature

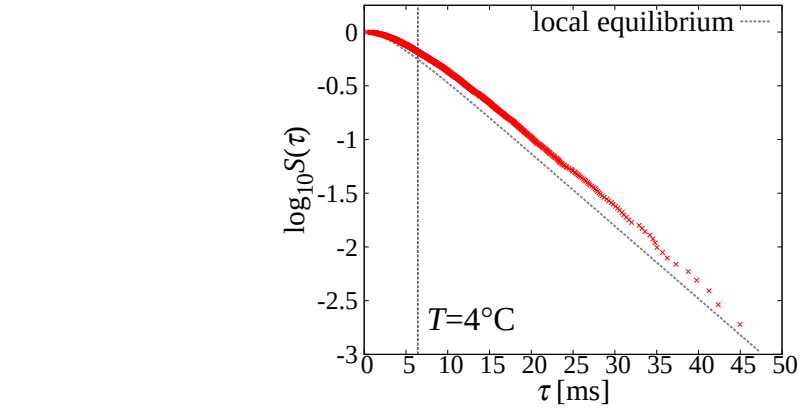

(a)

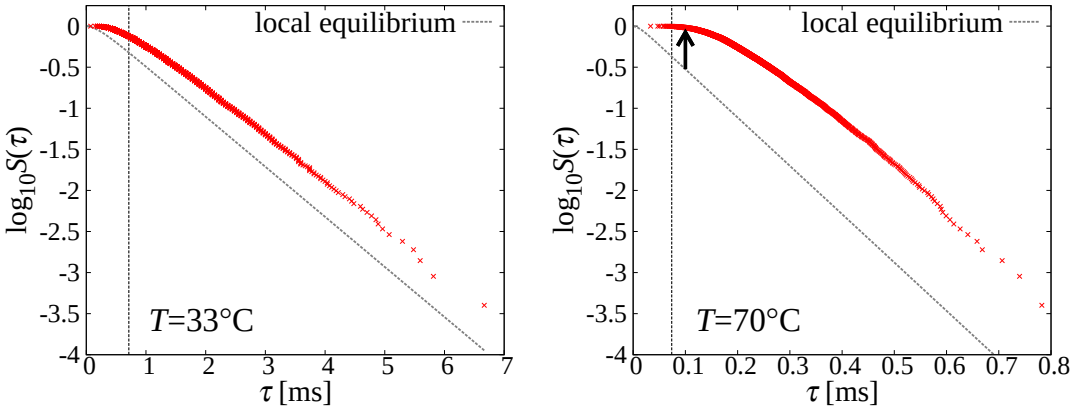

(b) (c)

Fig.3.12: The dwell time survival distributions at 4, 33, 70°C obtained by simulation (red). The grey broken lines show double exponential functions assuming fast diffusion limit $\bar{k}^{FDL}_{\mathrm{hyd/P_i}}$, i.e., the steady-state angle distributions equal to the Boltzmann distributions.

increases to 33°C and 70°C (Fig. 3.12(b) and (c), respectively), the deviation gets more evident. The remarkable point is how they deform and deviate. When we look at the region around the hydrolysis timescale, represented by $1/\bar{k}^{\mathrm{FDL}}_{\mathrm{hyd}} = 6.4, 0.71, 7.4\times10^{-2}$ms for 4, 33, and 70°C, respectively, the curvature of the survival distribution gets flatter, while at the longer time region than that the slope of the simulated curve gets close to parallel to the hypothetical one.[*1] This result corresponds to the negative correlation between the pre- and post-hydrolysis dwell time and, moreover, this effect contributes to fitting errors with multi-exponential functions. Actually, the dwell time distribution at temperature higher than 65°C could not be fitted with our method and the maximum temperature of the simulated rate coefficients is

[*1] It is possible that the population of the longer dwell time is also suppressed because the negative correlation appears when both pre- and post-hydrolysis dwell time cannot be longer than average at the same time. However, the two-body correlation of the two dwell time (Fig.3.9) shows that the negative correlation appears only for the short-short dwell time case and the correlation is almost zero for the long-long case.

60°C in the Arrhenius plot in Sec. 3.1.1 (Fig. 3.1).

Although the biomolecule working at the temperature higher than 60°C sounds to be unrealistic, we have to remark again that the F_1-ATPase we discussed in this study is derived from Thermophilic *Bacillus*, whose optimal temperature is 75°C. Our predictive result discussed above will propose a strong remark agains the conventional dwell time analysis when the single-molecule observation becomes possible at the temperature close to the physiological one of the protein in the future.

Chapter 4

Conclusion

4.1 Summary

In this study, we extended a potential switching (reaction-diffusion) model of a rotary protein motor F_1-ATPase adopted in R. Watanabe et al.(2013)[21] and C.-B. Li et al. (2015)[17] and after tuning the parameters based on experimental data we investigated how the rotary angle fluctuation changes with temperature and affects the chemical kinetics.

The model is Brownian motion of the rotary angle in stochastically switching potentials, which displays the step-wise rotation. The rate constants of the switching caused by chemical reactions (hydrolysis and P_i release) depends on the rotary angle, reflecting the chemo-mechanical coupling mechanism. This model has two important timescales: diffusion timescale to reach the local-equilibrium distribution in a potential and the reaction timescale to jump onto the next potential. In this study, we incorporated temperature dependence to the angle-dependent rate constants and the effective friction constants and numerically investigated how the relationship between these two timescales changes and affects the waiting time for reactions and the rate coefficients. As a result, we found that the rotary angle distributions get more deviated from the local-equilibrium ones for both pre- and post-hydrolysis dwells as the temperature increases. This increasing non-equilibrium property is brought about because the shortening of the reaction timescales surpasses that of diffusion timescale so that the system moves onto the next reactive potential before the local-equilibrium process during the dwell is accomplished.

As the steady state angle distributions during the pre- and post-hydrolysis dwells localize toward the smaller angle region, we found two phenomena which have not been reported in experiments.

First, the Arrhenius law breaks in the temperature dependence of the P_i release rate coefficient. As the activation free energy is higher at the smaller angle region, effective barrier height gets higher as the temperature increases and the system gets more non-equilibrium. This is why the slope of the Arrhenius plot gets smaller at higher temperature. Because the Arrhenius analysis has been done to estimate the activation enthalpy and entropy under the assumption of the Arrhenius law in preceding works, we proposed modified method to calculate the thermodynamic quantities from the static angle dependent rate constant rather than the rate coefficient obtained from the dynamical rotary assay. As a result, we found positive entropy change at P_i release contrary to the preceding work, which can be explained by the opening motion of the catalytic site without calculating the water entropy effect.

Second, increasing negative correlation was found between two successive reactions, hydrolysis and P_i release, during each catalytic dwell. This is because the memory of the rotary angle trajectory is carried into the next sub-dwell before it is lost by the local-equilibration. The independence of these two reactions has been implicitly assumed when their rate coefficients were obtained by the dwell time fitting with a double-exponential function. This result is consistent with the simulation result that the deformation of the dwell time distribution gets more significant around short dwell time region as the temperature increases. The double-exponential fitting becomes finally invalid at $60° > T$, which is close to the physiological temperature of the bacteria which the protein we used for parameter tuning is derived from ($\sim$75°C). We consider that our result proposes a caution against the conventional dwell time analysis when single molecule measurement experiment at such a high temperature becomes possible in the future.

The significance of this research lies in proposing a possible scenario which has never observed with current experimental technology. Our study is based on a simple one-dimensional model and it appears to be less similar to the real protein dynamics compared with molecular dynamics (MD) simulations. The merit of our model is, however, the number of physical parameters is much smaller and easier to tune preserving objectivity while MD simulations generally introduce a lot of objective parameters such as force fields between atoms. Moreover, MD simulations require so much calculation cost that long time scale simulations close to ms order are unrealistic. It is also quite difficult to collect enough samples to provide reliable statistics analysis. Although our results with a simple model do not guarantee quantitative accuracy especially at lower and higher temperature than room temperature, where we extrapolated the parameters in a rather artificial way due to the lack of information, we consider that they are qualitatively plausible because the parameters are inferred from the time series analysis of the real data as much as possible.

As well as our results suggest some remarks against conventional experimental analysis methods in the future, we also consider that our scenario should have constructive meanings when it is verified in experiments. The non-Arrhenius kinetics has been theoretically studied and considered to be due to the fluctuation of the activation free energy,[35,50,63,64] although its molecular origin has not been extensively discussed. Because our results suggest that it is due to the coupling of the diffusive non-equilibrium mechanical properties and the parallel reaction pathways along the rotary angle, experimental verification will increase the understanding of the physical origin of the non-Arrhenius kinetics. The correlation in catalytic waiting time in enzyme kinetics have also been theoretically studied[40–42] to explain the experiments[40,44–46] although it is pointed out that such experimental results could be due to the artifacts in the analysis of law S/N ratio data.[47] In this sense, verifying the correlation in F_1 kinetics in experiments will guarantee the significance of these theoretical studies.

4.2 Some Remarks on the Model Construction

In constructing the mathematical model in this study, we tuned the parameters based on the time series analysis so that the outcome is as consistent with the real data as possible. Although our results are meaningful in a sense that we propose a possible scenario, there is still a room for improvement

in model construction in order to increase the plausibility of our results and make more reasonable prediction. Especially, as to the extension to higher and lower temperature experimental data do not cover, we have to admit that the way of incorporating the temperature dependence does not have solid physical foundation because of the lack of further information.

In this section, we discuss the model construction and parameters again to clarify the future tasks.

4.2.1 Temperature Dependence

The temperature dependence is introduced to the angle-dependent rate constants and the effective friction.

The angle-dependent rate constants $k_i(\theta)$ eqn.(2.5) are determined under the assumption that the Arrhenius relation holds for each rotary angle θ. Although the Arrhenius law is believed to hold in several chemical reactions, there is no solid evidence that we can apply it in this case. It is possible that the angle-dependent rate constants also deviate from the Arrhenius law just as the rate coefficients obtained from the dwell time analysis showed non-Arrhenius temperature dependence. In order to make this point clear, the precise measurement with the stall-and-release experiment at different temperature is required.

As to the effective friction $\Gamma(T)$, we assumed that it has the same temperature dependence as that of pure water (Sec.2.4.3). This does not have evidence although the same method is applied in measuring the torque of the rotation at 4∼49°C after checking that the viscosity of the medium agreed with that of water within the error range of 5% under the temperature of 3∼25°C.[48] In the actual situation, the hydrodynamic effects near the glass surface and the internal degree of freedom can also come into the effective friction, which are taken into the proportionality constant C_η in a temperature-independent way. The internal degree of freedom can affect the effective friction in a form of the internal friction due to the dissipative interaction within a protein, e.g., the contact between the γ-subunit and the $(\alpha\beta)_3$-subunit, and that within α and β-subunits during conformational deformation. The internal friction of a protein has been studied for enzymes from the solvent friction dependence of the rate constants[65–70] but there is still no decisive methods to quantitatively measure it. In recent studies measuring the mechanical response to external electric force, the internal friction of an enzyme Guanylate kinase was measured by modeling a protein as a system in which a spring and a damper are connected in series, called Maxwell-type viscoelastic model.[71–74] They also measured the temperature dependence of the internal friction and showed that it gets smaller as temperature increases.[75] Although the quantities measured in this method could be model-dependent and there is still a room for scrutinizing their actual physical meaning, it may be possible to measure the internal friction of α, β-subunits and obtain some meaningful insight because the Guanylate kinase is similar to the β-subunit in respect to the size, structure, and the way of the conformational change. Measuring the internal friction of F_1-ATPase is important not only for the parameter determination but also from the view point of thermodynamic efficiency because so far it is measured only from the rotary degree of freedom.[2,3,76]

In addition to the angle-dependent rate constants and the effective friction, the curvature of the potential κ can also depend on temperature. Considering that the chemical bonds of a protein loosens,

we can expect that the restoring force of the protein conformation becomes weaker as temperature increases, resulting in lower κ. Actually in the study of the mechanical response measurement mentioned above, the elasticity of the protein was also measured and they showed that the stiffness parameter of the protein also decreases as temperature increases. If this expectation is true, the non-equilibrium effect is more enhanced because the relaxation time of the rotary angle fluctuation gets longer so that the rotary angle localizes at the region farther away from the bottom of the reactive potentials. In this study, however, we neglected the temperature dependence of this quantity because the curvature of a potential is difficult to measure. Although it can be inferred from the rotary angle distribution during dwells as explained in Sec.2.4.1, we have to artificially assume that the curvatures of the two types of reactive potentials, those of pre- and post-hydrolysis, are the same. In order to resolve them, we have to detect when the hydrolysis takes place during each catalytic dwell. Moreover, the rotary angle distribution itself can be easily affected by many experimental factors and it is difficult to obtain a stable value. For example, the rotation can deviate from a clean circle due to the local heterogeneity of the $(\alpha\beta)_3$-subunit, although we removed some of them whose deviation are too strong. Some data also show a rotation close to an ellipse, which suggests that the rotation plane is tilted and not parallel to the glass surface possibly due to the asymmetric interaction between the $(\alpha\beta)_3$-subunit and the γ-subunit or unstable attachment of a probe bead to the γ-subunit. Actually, we calculated the dwell angle distribution from the data and obtained the distribution width but they are so scattered that we could not judge whether they have temperature dependence or not. In order to overcome these problems, we need much more data sets and more strict data selection criteria.

4.2.2 Parameter Tuning of the Effective Friction

One more thing we have to take care of is the estimation of the effective friction.

In order to determine $\Gamma(T)$ from experimental data, we calculated the autocorrelation function of the rotary angle during dwells and looked at its exponent. In the case of the Brownian motion in a single harmonic potential, the autocorrelation decay follows a single exponential function. However, the experimental data obeys a double exponential function. As explained in Sec.2.4.3, we considered that the longer time constant is due to the two-step kinetics with 20° angle shift and that the shorter one is the local-equilibrium relaxation timescale $\tau_{\rm rel} = \Gamma/\kappa$ because the order of this value coincides with that calculated from κ determined from the rotary angle distribution and Γ calculated from eqn.(2.14) with water viscosity. If we have a mathematical relationship between the two relaxation time constants and other physical parameters especially the relaxation time constant and the reaction time constants, we will be able to obtain a more accurate value.

Furthermore, we have to consider whether the system can really be described by a white noise Langevin equation. If the relaxation of the solvent or the internal degree of freedom is slower than the motion of the bead, it is possible that the friction term becomes time-dependent and the system is described by a generalized Langevin equation.[29,77] Some theoretical cases are reported that a protein or a polymer chain has memory and must be described by a non-Markovian generalized Langevin equation.[78,79] The result of the mechanical response experiment mentioned in the previous subsection also suggests that the

protein has a time-dependent friction kernel.[72,73] In such systems, it is shown that the autocorrelation function does not necessarily obey a single exponential function,[78] which means that we can obtain meaningless value by linear fitting of the log-linear plot of an autocorrelation function. In order to avoid such artifacts, we have to scrutinize the rheological property of the protein.

4.3 Future Perspectives

This study started from one question: how does fluctuation affect the behavior of biomolecules? Here we found that in the F_1-ATPase its chemical kinetics can be changed by temperature and that some of the conventional data analysis methods could produce unexpected values.

As future studies, we propose some directions to advance this theme.

4.3.1 Experimental Verification

So far, we only proposed a theoretical prediction. Then the next step is experimental verification. The most direct way is to observe F_1 at higher temperature but it is difficult from the technological view point. Although the maximum temperature reported for single molecule observation is 40°C.,[48] where the negative correlation between hydrolysis and P_i release waiting time begins to appear, it is still not enough considering the experimental error is expected to affect the result. For this reason, we have to wait for the technological development to prove our prediction directly.

Then, we consider another way to induce non-equilibrium angle fluctuation and its effect on kinetics. There are two ways. First, we can increase the friction on the rotary probe and make the diffusion timescale longer by tethering a larger probe. Second, we can increase the ATP concentration and make the reaction timescale of ATP binding shorter. If we can make the two timescales competitive by these ways, non-equilibrium angle fluctuation is expected to emerge. It could be verified by observing how the rotary angle distribution during a dwell changes although the change point detection of the rotary time series may be difficult when we increase the probe friction. If we make a non-equilibrium state, however, there is a problem in observing its effect on kinetics. Under the same temperature, the thing we have to look at is the correlation between the waiting time for successive reactions. The problem is that we cannot tell when each reaction happens during a dwell from a experimental time series. If we focus on the catalytic dwell, we have to know at which time instant hydrolysis takes place during a dwell but it is quite difficult to spot out because the $\sim 20^\circ$ rotation is concealed by the thermal fluctuation. In the binding dwell, ATP binding and the temperature sensitive (TS)[12] step take place but it is even difficult to know which reaction happens at which instant because detail of the TS step is still unknown. One possible key to solve this problem can be the autocorrelation decay of the rotary angle during a dwell. In the catalytic dwell, the autocorrelation function is not single exponential as expected from simple brownian motion in a single harmonic potential, but is double exponential as shown in Sec. 2.4. If our speculation is correct and the longer time constant originates from the two-step kinetic scheme of hydrolysis and P_i release, this decay function may change with or without the correlation. In addition to this indirect approach, it would be effective to consider the way to speculate when hydrolysis takes place

during a dwell from the time series. Assuming the Langevin potential switching dynamics, the switching angle could be speculated by Byes statistics, for example.

4.3.2 Effects of the Fluctuation on Thermodynamic Efficiency

In this work we focused only on the chemical kinetics and did not touch the relationship with enzyme function. Because the most remarkable point of the F_1-ATPase is its high energy conversion efficiency,[76,80] we would like to work on how the fluctuation affects the energy transduction mechanism. Because the corporation of the three $(\alpha\beta)$-subunit pairs intermediated by the γ-subunit enhances the catalytic performance, it should also contribute to the energy efficiency. Especially, the correlation we found between different reactions, which are considered to take place at different catalytic sites, can be interpreted as follows; one of the reactions acquires the information of the chemical state of another and the feedback-control mechanism is established. Recently, the study of the relationship between thermodynamic quantities and information, called information thermodynamics, is developed and especially the second law of thermodynamics in fluctuating system is expanded to include the information entropy. Its application to biological system is also proceeding[81] and we consider it interesting to investigate how the corporative motion of different subunits contributes to the energy conversion efficiency in F_1-ATPase.

4.3.3 Application to Other Protein Motor Systems

It is also interesting point to investigate the universality of the non-equilibrium effects on the chemical kinetics of other protein motor systems. The key point of our work is the timescale competition between the chemical reaction and another degree of freedom which controls the reaction. There are many kinds of protein motor systems besides F-ATPase[82] such as V-ATPase[83,84] and linear motors walking on filaments[85]. If these proteins also have such properties, it is possible that anomalous kinetics take place under some circumstances and that some data analysis methods should be modified.

Appendix

A.1 Langevin Equation and Fokker-Planck Representation

A.1.1 Overdamped Limit

The common form of the Langevin equation in physics is a second order one with a frictional force $-\eta\frac{dx}{dt}$ and a potential force $-dU(x)/dx$

$$\begin{aligned} m\frac{d^2x}{dt^2} &= -\eta\frac{dx}{dt} - \frac{dU(x)}{dx} + \sqrt{2D}\xi(t), \\ \langle\xi(t)\rangle = 0, &\quad \langle\xi(0)\xi(t)\rangle = \delta(t), \end{aligned} \tag{A.1}$$

where m, η, D are the mass of the particle, the friction constant, and the diffusion constant, respectively. $\xi(t)$ is a Gaussian white noise and the bracket $\langle\cdot\rangle$ means the ensemble average over the possible noise realization. This is widely used in simulating the motion of nano-size matters (pollen grains, beads, biomolecules, ...etc.) susceptible to thermal noise.

When the ratio of m and η is much smaller than the observation timescale, the second-order derivative term can be neglected and we can reduce it into a first order equation

$$\eta\frac{dx}{dt} = -\frac{dU(x)}{dx} + \sqrt{2D}\xi(t). \tag{A.2}$$

This is called the overdamped limit. Apparently we can obtain it by simply taking $m \to 0$ but we show it in detail to discuss its scope of application.

The following discussion is based on the books by R.Zwanzig (2001) [30] and K.Sekimoto (2010). [86] First, we rewrite eqn.(A.1) with the momentum $p(t)$ as

$$\frac{dx(t)}{dt} = p(t)/m, \tag{A.3a}$$

$$\frac{dp(t)}{dt} = -\frac{dU(x)}{dx} - \frac{\eta}{m}p(t) + F_p(t), \tag{A.3b}$$

where $F_p(t) = \sqrt{2D}\xi(t)$ is a random force of the momentum satisfying

$$\langle F_p(t)\rangle = 0, \tag{A.4a}$$

$$\langle F_p(0)F_p(t)\rangle = 2D\delta(t). \tag{A.4b}$$

We solve it formally as

$$\begin{aligned} p(t) &= e^{-\frac{\eta}{m}t}p(-\infty) + \int_{-\infty}^{t} e^{-\frac{\eta}{m}(t-s)}\left\{-\frac{dU(x(s))}{dx} + F_p(s)\right\}ds \\ &= \int_{\infty}^{0} e^{-\frac{\eta}{m}s}\left\{-\frac{dU(x(t-s))}{dx} + F_p(t-s)\right\}ds, \end{aligned} \tag{A.5}$$

and obtain

$$\frac{dx(t)}{dt} = -\frac{1}{m}\int_0^\infty e^{-\frac{\eta}{m}s}\frac{dU(x(t-s))}{dx}ds + \tilde{F}_x(t), \tag{A.6}$$

where the second term in the right hand side is the random force and represented as

$$\tilde{F}_x(t) = \frac{1}{m}\int_0^\infty e^{-\frac{\eta}{m}s}F_p(t-s)ds.$$

Here we assume that the momentum at $t \to 0$ is zero $p(-\infty) = 0$. We then calculate the noise average of this force and its autocorrelation.

$$\langle\tilde{F}_x(t)\rangle = \left\langle\frac{1}{m}\int_0^\infty e^{-\frac{\eta}{m}s}F_p(t-s)ds\right\rangle = \frac{1}{m}\int_0^\infty e^{-\frac{\eta}{m}s}\langle F_p(t-s)\rangle ds = 0.$$

Here we used eqn.(A.4a). We calculate the autocorrelation assuming $t < t'$ as follows;

$$\begin{aligned}
\langle\tilde{F}_x(t)\tilde{F}_x(t')\rangle &= \left\langle\frac{1}{m^2}\int_0^\infty\int_0^\infty e^{-\frac{\eta}{m}(s+s')}F_p(t-s)F_p(t'-s')dsds'\right\rangle \\
&= \frac{1}{m^2}\int_{-\infty}^{t} ds\int_{-\infty}^{t'} ds' e^{-\frac{\eta}{m}\{(t-s)+(t'-s')\}}\langle F_p(s)F_p(s')\rangle \\
&= \frac{2D}{m^2}\int_{-\infty}^{t} e^{-\frac{\eta}{m}(t+t'-2s)}ds \quad (\because \text{eqn.(A.4b)},\ (-\infty,t') \ni \forall s \in (-\infty,t)) \\
&= \frac{D}{m\eta}e^{-\frac{\eta}{m}(t'-t)}.
\end{aligned}$$

Therefore, we can sum them up as

$$\langle\tilde{F}_x(t)\rangle = 0, \tag{A.7a}$$

$$\langle\tilde{F}_x(t)\tilde{F}_x(t')\rangle = \frac{D}{m\eta}e^{-\frac{\eta}{m}|t-t'|}. \tag{A.7b}$$

The second equation used the symmetry of t and t'. This relationship shows that the random noise $\tilde{F}_x(t)$ is a colored noise. From the discussion above, the ratio of m and η, $\tau_p = m/\eta$, corresponds to the correlation decay timescale of the noise $\tilde{F}_x(t)$ or the momentum $p(t)$. When this value is small enough compared with the observation timescale and we can regard $\tau_p \to 0$, the autocorrelation function eqn.(A.7b) becomes a delta function and we can approximate $\tilde{F}_x(t)$ as a white noise

$$\langle\tilde{F}_x(t)\tilde{F}_x(t')\rangle \to \frac{2D}{\eta^2}\delta(t-t')$$

because of the relationship

$$ae^{-a|x|} \xrightarrow{a\to\infty} 2\delta(x).$$

In the same way, the left hand side of eqn.(A.6), the Langevin equation of $x(t)$, can also be represented as

$$\begin{aligned}
-\frac{1}{m}\int_0^\infty e^{-\frac{\eta}{m}s}\frac{dU(x(t-s))}{dx}ds &\xrightarrow{\eta/m\to\infty} -\frac{1}{\eta}\int_0^\infty 2\delta(s)\frac{dU(x(t-s))}{dx}ds \\
&= -\frac{1}{\eta}\frac{dU(x(t))}{dx}.
\end{aligned} \tag{A.8}$$

In all, when $\eta/m \to \infty$, the Langevin equation eqn.(A.1) becomes

$$\eta \frac{dx(t)}{dt} = -\frac{dU(x)}{dx} + F_x(t) \tag{A.9}$$

with a random noise $F_x(t)$ satisfying

$$\langle F_x(t) \rangle = 0, \quad \langle F_x(0) F_x(t) \rangle = 2D\delta(t).$$

This is exactly the overdamped limit eqn.(A.2). In this limit, the momentum $p(t)$ (eqn.(A.5)) is a fast variable and erased from the equation. Even if the mass of the particle m has a finite value, the overdamped limit can be verified as an approximation when the time resolution of the observation is much longer (coarser) than $\tau_p = m/\eta$, the relaxation time of the random noise autocorrelation eqn.(A.7b).[86,87] Actually, we can safely use this limit to model the movement of a gold nano particle (ϕ=80nm) tethered to a protein because $m \approx 5 \times 10^{-21}$kg and $\eta \approx 7 \times 10^{-10}$kg/s so that $\tau_p \approx 7$ps, which is much shorter than 1$\sim$ 40µs, the time resolution of the experiment.

A.1.2 Fluctuation-Dissipation Relation

In the Langevin equation eqn.(A.1), it is sometimes wrongly understood that the random force term $\sqrt{2D}\xi(t)$ is the collisional force of the surrounding molecules to the Brownian particle. It is partly true but the frictional force term $-\eta\frac{dx}{dt}$ also originates from the collision. The random force is the mean force due to the molecular collision forces averaged within a mesoscopic timescale. Because both random force and frictional force terms share the same origin, there is an important relation between the friction constant η and the diffusion constant D called the fluctuation dissipation relation. When the thermal equilibrium is attained between the surrounding media and the Brownian particle, the relation below holds;

$$D = \eta k_B T, \tag{A.10}$$

where k_B and T are the Boltzmann constant and the temperature, respectively.

In the case of free Brownian motion without a potential $U(x)$, this can be easily derived by assuming the equipartition of the energy between the Brownian particle and the surrounding molecules, i.e., $m\langle u(t)^2 \rangle/2 = k_B T/2$, where $u(t) = dx(t)/dt$ is the velocity and the bracket $\langle \cdot \rangle$ is the ensemble average over possible noise realization. The Langevin equation is as follows;

$$\begin{aligned} m\frac{du(t)}{dt} &= -\eta u(t) + \sqrt{2D}\xi(t), \\ \langle \xi(t) \rangle &= 0, \quad \langle \xi(0)\xi(t) \rangle = \delta(t). \end{aligned} \tag{A.11}$$

We can solve this equation in a formal way as below;

$$u(t) = u(0)e^{-\frac{\eta}{m}t} + \frac{\sqrt{2D}}{m}\int_0^t e^{-\frac{\eta}{m}(t-s)}\xi(s)ds. \tag{A.12}$$

From this equation, the autocorrelation function of $u(t)$ is calculated as

$$\begin{aligned} \langle u(t)u(t') \rangle &= \langle u(0)^2 \rangle e^{-\frac{\eta}{m}(t+t')} + \frac{2D}{m^2}\int_0^t \int_0^{t'} e^{-\frac{\eta}{m}(t+t'-s-s')} \langle \xi(s)\xi(s') \rangle ds ds' \quad \cdots (*) \\ &= \langle u(0)^2 \rangle e^{-\frac{\eta}{m}(t+t')} + \frac{D}{m\eta}\left\{ e^{-\frac{\eta}{m}|t-t'|} - e^{-\frac{\eta}{m}(t+t')} \right\}. \end{aligned} \tag{A.13}$$

By setting $t = t'$ and substituting $\langle u(t)^2 \rangle = \langle u(0)^2 \rangle = k_B T/m$, we obtain eqn.(A.10) and

$$\langle u(t)u(t') \rangle = \frac{k_B T}{m} e^{-\frac{\eta}{m}|t-t'|}. \tag{A.14}$$

The second term in (*) is calculated as follows; when $t > t'$,

$$\begin{aligned}
\frac{2D}{m^2} \int_0^t \int_0^{t'} e^{-\frac{\eta}{m}(t+t'-s-s')} \langle \xi(s)\xi(s') \rangle ds ds' &= \frac{2D}{m^2} \int_0^t \int_0^{t'} e^{-\frac{\eta}{m}(t+t'-s-s')} \delta(s-s') ds ds' \\
&= \frac{2D}{m^2} \int_0^t e^{-\frac{\eta}{m}(t+t'-2s)} ds \\
&= \frac{D}{m\eta} \left\{ e^{-\frac{\eta}{m}(t-t')} - e^{-\frac{\eta}{m}(t+t')} \right\}.
\end{aligned}$$

Taking the case $t' \leq t$ into account, we obtain the equation above.

If the particle is trapped in a potential, the fluctuation dissipation relation can also be derived in the same way if the potential is harmonic $U(x) = kx^2/2$ and the overdamped limit is verified;

$$\eta \frac{dx(t)}{dt} = -kx(t) + \sqrt{2D}\xi(t). \tag{A.15}$$

This equation is in the exactly same form as eqn.(A.11) and by assuming the equipartition of the energy $\langle kx(t)^2/2 \rangle = k_B T/2$ we can obtain the relation $D = \eta k_B T$ in the same way. In this case the autocorrelation decay of $x(t)$ follows

$$\langle x(t)x(t') \rangle = \frac{k_B T}{k} e^{-\frac{k}{\eta}|t-t'|}. \tag{A.16}$$

The Brownian motion described by a linear first-order Langevin equation such as eqn.(A.11) and (A.15) is called Ornstein-Uhlenbeck process. Even if the overdamped limit cannot be applied, the same fluctuation dissipation relation is obtained although the derivation is more complicated by using the Wiener-Khinchin theorem.[29,77]

A.1.3 Derivation of the Fokker-Planck Equation

While the Langevin equation describes a trajectory of a Brownian motion, the Fokker-Planck equation is the time evolution equation of its distribution. Given a general form of the one-dimensional Langevin equation

$$dX(t) = a(X,t)dt + b(X,t)dB(t), \tag{A.17}$$

where $B(t)$ is the Wiener process, its Fokker-Planck equation is;

$$\frac{\partial P(X;t)}{\partial t} = -\frac{\partial}{\partial X} \{a(X,t)P(X;t)\} + \frac{1}{2} \frac{\partial^2}{\partial X^2} b(X,t)^2 P(X;t). \tag{A.18}$$

$P(X;t)$ is the probability distribution of X at time t. In order to derive it,[88] we consider the conditional probability $P(X;t|X_0;t_0)$ with the initial condition $X(t = t_0) = X_0$. By using the Chapman-Kolmogorov equation, we obtain

$$P(X;t+\Delta t|X_0;t_0) = \int P(X;t+\Delta t|Y;t)P(Y;t|X_0;t_0)dY \tag{A.19}$$

for $\Delta t > 0$. Using it with an arbitrary function $f(X)$,

$$\begin{aligned}\int f(X)\left\{P(X;t+\Delta t|X_0;t_0)-P(X;t|X_0;t_0)\right\}dX \\ = \int dX f(X)\int dY P(X;t+\Delta t|Y;t)P(Y;t|X_0;t_0)-\int dY f(Y)P(Y;t|X_0;t_0).\end{aligned} \tag{A.20}$$

Considering that $|X-Y|$ is small enough when Δt is infinitesimal, we apply the Taylor expansion to $f(X)$ and truncate it at the second order;

$$f(X)\approx f(Y)+\frac{df(Y)}{dY}(X-Y)+\frac{1}{2}\frac{d^2f(Y)}{dY^2}(X-Y)^2. \tag{A.21}$$

Substituting it into the first term of the left hand side of eqn.(A.20),

$$\begin{aligned}\int dX f(X)\int dY P(X;t+\Delta t|Y;t)P(Y;t|X_0;t_0) \\ = \int dY f(Y)P(Y;t|X_0;t_0)\int dX P(X;t+\Delta t|Y;t) \\ + \int dY \frac{df(Y)}{dY}P(Y;t|X_0;t_0)\int dX(X-Y)P(X;t+\Delta t|Y;t) \\ + \int dY \frac{1}{2}\frac{d^2f(Y)}{dY^2}P(Y;t|X_0;t_0)\int dX(X-Y)^2P(X;t+\Delta t|Y;t).\end{aligned} \tag{A.22}$$

Considering that X, Y obey the Langevin equation eqn.(A.17), the spatial displacement $\Delta X = X - Y$ during the small time interval Δt is

$$\Delta X \approx a(Y,t)\Delta t + b(Y,t)\Delta B(t), \tag{A.23}$$

where $\Delta B(t) = B(t+\Delta t) - B(t)$. Using this relation, we obtain

$$\int dX(X-Y)P(X;t+\Delta t|Y;t) = \langle \Delta X\rangle = a(Y,t)\Delta t, \tag{A.24a}$$

$$\int dX(X-Y)^2P(X;t+\Delta t|Y;t) = \langle (\Delta X)^2\rangle \approx b(Y,t)^2\Delta t. \tag{A.24b}$$

In the second equation, we truncated higher order terms than Δt. Substituting these two into eqn.(A.22), it becomes

$$\begin{aligned}\int dX f(X)\int dY P(X;t+\Delta t|Y;t)P(Y;t|X_0;t_0) \\ = \int dY f(Y)P(Y;t|X_0;t_0)\int dX P(X;t+\Delta t|Y;t) \\ + \Delta t\int dY \frac{df(Y)}{dY}a(Y,t)P(Y;t|X_0;t_0) + \Delta t\int dY\frac{1}{2}\frac{d^2f(Y)}{dY^2}b(Y,t)^2P(Y;t|X_0;t_0) \\ = \int dY f(Y)P(Y;t|X_0;t_0) \\ + \Delta t\int dY f(Y)\left[-\frac{\partial}{\partial Y}\left\{a(Y,t)P(Y;t|X_0;t_0)\right\}+\frac{1}{2}\frac{\partial^2}{\partial Y^2}\left\{b(Y,t)^2P(Y;t|X_0;t_0)\right\}\right].\end{aligned} \tag{A.25}$$

From the second to the third equation, we partially integrated the derivatives of $f(Y)$. As a result, eqn.(A.20) becomes

$$\frac{1}{\Delta t}\int dX f(X)\left\{P(X;t+\Delta t|X_0;t_0)-P(X;t|X_0;t_0)\right\} \\ =\int dX f(X)\left[-\frac{\partial}{\partial X}\left\{a(X,t)P(X;t|X_0;t_0)\right\}+\frac{1}{2}\frac{\partial^2}{\partial X^2}\left\{b(X,t)^2P(X;t|X_0;t_0)\right\}\right]. \tag{A.26}$$

Because $f(X)$ is arbitrary, by taking $\Delta t\to 0$ we obtain the Fokker-Planck equation

$$\frac{\partial P(X;t|X_0;t_0)}{\partial t}=-\frac{\partial}{\partial X}\left\{a(X,t)P(X;t|X_0;t_0)\right\}+\frac{1}{2}\frac{\partial^2}{\partial X^2}\left\{b(X,t)^2P(X;t|X_0;t_0)\right\}. \tag{A.27}$$

If we consider a high-dimensional case

$$dX_i(t)=a_i(\boldsymbol{X},t)dt+\sum_j b_{ij}(\boldsymbol{X},t)dB_j(t), \tag{A.28}$$

its Fokker-Planck counterpart is;

$$\frac{\partial P(\boldsymbol{X};t)}{\partial t}=-\sum_i\frac{\partial}{\partial X_i}\left\{a_i(\boldsymbol{X},t)P(\boldsymbol{X};t)\right\}+\frac{1}{2}\sum_{i,j}\frac{\partial}{\partial X_i}\frac{\partial}{\partial X_j}B_{ij}(\boldsymbol{X},t)P(\boldsymbol{X};t), \tag{A.29}$$

where $B_{ij}(\boldsymbol{X},t)=\sum_k b_{ik}(\boldsymbol{X},t)b_{jk}(\boldsymbol{X},t)$. In the case of the physically common underdamped Langevin equation, i.e, eqn.(A.1) and (A.3), the corresponding Fokker-Planck equation is

$$\frac{\partial P(x,p;t)}{\partial t}=-\frac{\partial}{\partial x}\left\{\frac{p}{m}P(x,p;t)\right\}-\frac{\partial}{\partial p}\left\{-\frac{dU(x)}{dx}-\frac{\eta}{m}p\right\}P(x,p;t)+D\frac{\partial^2}{\partial p^2}P(x,p;t), \tag{A.30}$$

while the overdamped limit eqn.(A.2) is represented by the Smolchowski equation

$$\frac{\partial P(x;t)}{\partial t}=-\frac{\partial}{\partial x}\left\{-\frac{1}{\eta}\frac{dU(x)}{dx}P(x;t)\right\}+\frac{D}{\eta^2}\frac{\partial^2}{\partial x^2}P(x;t). \tag{A.31}$$

A.2 Numerical Calculation Method of the Potential Switching Model

In this section, we explain the numerical method to calculate the potential switching model (eqn.(2.7a)). The calculation consists of two parts; numerical solution of the Langevin equation and potential switching.

An overdamped Langevin equation is numerically solved by a finite difference method.[89,90] Here, we calculate it with time step Δt. First, we rewrite the equation into a differential form as below;

$$d\theta(t)=-\frac{1}{\Gamma}\frac{dG^{\mathrm{pre/post}}(\theta(t))}{d\theta}dt+\sqrt{\frac{k_BT}{\Gamma}}dB(t). \tag{A.32}$$

By simply integrating it with t over $[t,t+\Delta t]$, we obtain

$$\theta(t+\Delta t)-\theta(t)=-\frac{1}{\Gamma}\int_t^{t+\Delta t}\frac{dG^{\mathrm{pre/post}}(\theta(s))}{d\theta}ds+\sqrt{\frac{k_BT}{\Gamma}}B(\Delta t), \tag{A.33}$$

where $B(\Delta t) = \int_t^{t+\Delta t} dB(s) = B(t+\Delta t) - B(t)$ obeys the Gaussian distribution with zero mean and $\sqrt{\Delta t}$ standard deviation. By approximating the first term of the right hand side as

$$-\frac{1}{\Gamma}\int_t^{t+\Delta t} \frac{dG^{\mathrm{pre/post}}(\theta(s))}{d\theta} ds \approx -\frac{1}{\Gamma}\frac{dG^{\mathrm{pre/post}}(\theta(t))}{d\theta}\Delta t, \tag{A.34}$$

we obtain the Euler-Maruyama scheme;

$$\theta_{t+\Delta t} = \theta_t - \frac{\Delta t}{\Gamma}\frac{dG^{\mathrm{pre/post}}(\theta_t)}{d\theta} + \sqrt{\frac{k_B T}{\Gamma}} B(\Delta t). \tag{A.35}$$

It is the simplest scheme to numerically solve a stochastic differential equation and its precision is the order of $(\Delta t)^{\frac{1}{2}}$. In this study, however, we used an improved higher order method, Heun scheme shown below, with 1st order precision of Δt

$$\begin{aligned} \bar{\theta}_t &= \theta_t - \frac{\Delta t}{\Gamma}\frac{dG^{\mathrm{pre/post}}(\theta_t)}{d\theta} + \sqrt{\frac{k_B T}{\Gamma}} B(\Delta t) \\ \theta_{t+\Delta t} &= \theta_t - \frac{1}{2}\frac{\Delta t}{\Gamma}\left\{\frac{dG^{\mathrm{pre/post}}(\theta_t)}{d\theta} + \frac{dG^{\mathrm{pre/post}}(\bar{\theta}_t)}{d\theta}\right\} + \sqrt{\frac{k_B T}{\Gamma}} B(\Delta t). \end{aligned} \tag{A.36}$$

The two Gaussian noises $B(\Delta t)$ are the same ones.

For each time step, we calculate the switching probability and determine whether to switch to the next potential or not with the Monte-Carlo method. The switching probability $P_{\Delta t}^{(i)}$, that is, the transition probability to the next potential during the time interval $[t, t+\Delta t]$, can be obtained as below in a formal expression;

$$P_{\Delta t}^{(i)} = 1 - \exp\left\{-\int_t^{t+\Delta t} k_i(\theta(s)) ds\right\}. \tag{A.37}$$

i indicates the pre- or post-hydrolysis dwell. It is the probability of trajectories escaping from the dwell during the time interval $[t, t+\Delta t]$ with the initial condition $\theta(t)$ without counting the returning ones or newly coming ones. When Δt is small enough, it is simply approximated as $k_i(\theta_t)\Delta t$ by assuming that the rate constant $k_i(\theta(t))$ does not change during this time interval and that $k_i(\theta_t)\Delta t$ is also small enough to approximate as $1 - \exp\{-k_i(\theta_t)\Delta t\} \approx k_i(\theta_t)\Delta t$. However, considering the case when $k_i(\theta(t))$ is sensitive to θ and its value is large, we provide a more precise method by assuming that $\theta(t)$ moves with linear uniform motion with velocity

$$v_t = \frac{\theta_{t+\Delta t} - \theta_t}{\Delta t}.$$

Thus, we obtain another approximation of the transition probability as below;

$$\begin{aligned} P_{\Delta t}^{(i)} &= 1 - \exp\left\{-\int_t^{t+\Delta t} k_i(v_t s + \theta_t) ds\right\} \\ &= 1 - \exp\left\{-k(\theta_t)\frac{\exp(\alpha_i v_t \Delta t) - 1}{\alpha_i v_t}\right\}. \end{aligned} \tag{A.38}$$

α_i is the angle dependence parameter in eqn.(2.5). It coincides with $k_i(\theta_t)\Delta t$ when $\alpha_i v_t \Delta t$ is small enough to consider $\exp(\alpha_i v_t \Delta t) \approx 1 + \alpha_i v_t \Delta t$. It may be possible that we can obtain the exact solution of eqn.(A.37) by the path integral method.

In the calculation, the time step Δt must not be too large compared with the typical timescale of the system. In this study, we set it so that $\tau_{\rm rel}/100 > \Delta t$, which means that it takes at least 100 time steps before the local-equilibrium relaxation time $\tau_{\rm rel} = \Gamma/\kappa$ in the potential. Besides the numerical calculation time step, we also set the output time step. It corresponds to the time resolution of the observation and is set to be the same as the experiment in which the data we use were obtained for $T \leqq 33$°C; 27000 fps (frames per second), about 40 µs/frame.[21] At higher temperature, we adopted 108000 fps (∼1µs/frame) following the recent experiments.

A.3 Mathematical Representation of the Dwell Time Distribution

Although the numerical calculation in this study is based on the Langevin equation, the dwell time distribution can also be described by the Fokker-Planck representation although it might be difficult to solve directly.

A.3.1 Simpler Case: Single Potential Switching Model

First, we show it in the case of a simpler model, a single potential switching model (2.2). Because the dwell time distribution is the escape time distribution from a potential, we first focus only on a single escape event neglecting the returning trajectories due to the potential switching. Based on the Agmon-Hopfield model (1.25), the dwell time distribution $S(\tau)$ can be represented as follows according to eqn.(1.27)

$$S(\tau) = \left\langle \exp\left\{ -\int_0^\tau k(\theta(s))ds \right\} \right\rangle_\theta . \tag{A.39}$$

The bracket $\langle\cdot\rangle_\theta$ is the ensemble average over all possible trajectories escaping from the potential at time τ.

While this is only a formal solution, which could be solved by the path-integral method, we can also calculate the dwell time distribution from the Fokker-Planck representation (Agmon-Hopfield equation (1.28)):

$$\frac{\partial C(\theta;t)}{\partial t} = -\frac{\partial}{\partial\theta}\left\{ -\frac{1}{\Gamma}\frac{dU(\theta)}{d\theta}C(\theta;t) \right\} + \frac{k_B T}{\Gamma}\frac{\partial^2}{\partial\theta^2}C(\theta;t) - k(\theta)C(\theta;t). \tag{A.40}$$

We have to solve it under a certain initial condition and its escape time survival distribution $S(\tau)$ can be obtained as $S(\tau) = \int C(\theta;\tau)d\theta$. Coming back to the model with returning trajectories, the initial angle distribution corresponds to the steady state landing angle distribution. The landing angle is the angle at which a trajectory returns and lands on to the potential after it escaped from it. When the angle shift after the switching is θ_b, the steady state landing angle distribution $P_{\rm land}(\theta)$ and the steady state escape angle distribution $P_{\rm es}(\theta)$ are related as

$$P_{\rm land}(\theta) = P_{\rm es}(\theta + \theta_b). \tag{A.41}$$

Meanwhile, the escape angle distribution is proportional to $k(\theta)P(\theta;t)$ and in the steady state it can be obtained as

$$P_{\rm es}(\theta) = \frac{k(\theta)P_{\rm st}(\theta)}{\int k(\theta')P_{\rm st}(\theta')d\theta'}, \tag{A.42}$$

where $P_{\rm st}(\theta)$ is the steady state angle distribution obtained by eqn.(2.3). In all, by using $C(\theta; t = 0) = P_{\rm es}(\theta + \theta_b)$ as the initial condition and solving eqn.(A.40), we obtain the dwell time distribution without directly taking the ensemble average among a number of trajectories produced by the Langevin equation.

A.3.2 F_1 Catalytic Dwell Model

In the case of the model with two potentials for the simulation of F_1-ATPase in this study, the catalytic dwell time distribution can be obtained in almost the same way as above from the Fokker-Planck representation (2.4). What we have to do is to solve the equations without returning paths after P_i release

$$\begin{aligned}\frac{\partial C^{\rm pre}(\theta;t)}{\partial t} &= -\frac{\partial}{\partial\theta}\left\{-\frac{1}{\Gamma(T)}\frac{dU^{\rm pre}(\theta)}{d\theta}C^{\rm pre}(\theta;t)\right\} + \frac{k_BT}{\Gamma(T)}\frac{\partial^2}{\partial\theta^2}C^{\rm pre}(\theta;t) \\ &\quad - k_{\rm hyd}(\theta;T)C^{\rm pre}(\theta;t), \end{aligned} \tag{A.43a}$$

$$\begin{aligned}\frac{\partial C^{\rm post}(\theta;t)}{\partial t} &= -\frac{\partial}{\partial\theta}\left\{-\frac{1}{\Gamma(T)}\frac{dU^{\rm post}(\theta)}{d\theta}C^{\rm post}(\theta;t)\right\} + \frac{k_BT}{\Gamma(T)}\frac{\partial^2}{\partial\theta^2}C^{\rm post}(\theta;t) \\ &\quad - k_{\rm P_i}(\theta;T)C^{\rm post}(\theta;t) + k_{\rm hyd}(\theta;T)C^{\rm pre}(\theta;t), \end{aligned} \tag{A.43b}$$

under the initial condition

$$C^{\rm pre}(\theta;0) = \frac{k_{\rm P_i}(\theta)P^{\rm post}_{\rm st}(\theta)}{\int k_{\rm P_i}(\theta')P^{\rm post}_{\rm st}(\theta')d\theta'}, \tag{A.44a}$$

$$C^{\rm post}(\theta;0) = 0, \tag{A.44b}$$

where $P^{\rm post}_{\rm st}(\theta)$ is the steady state solution of the model with returning trajectories (2.4).

Acknowledgement

First of all, I would like to express my greatest appreciation to Prof. Chun-Biu Li in Stockholm University, who has been my supervisor since I came to Hokkaido University. I tremendously owe my study in the doctor course to the fruitful discussion with him and his advice for both science and my career. I would also like to thank Prof. Tamiki Komatsuzaki and Prof. Hiroshi Teramoto, who have also been my advisors for four years. I would also like to thank my collaborators, Prof. Noji Hiroyuki and Dr. Rikiya Watanabe in the University of Tokyo. Without their experimental data and sophisticated comments, this research could not be accomplished. I would also express my gratitude to all the professors and staffs of the department of mathematics in Hokkaido University, especially to Prof. Zin Arai, who was my supervisor for a while and is now in Chubu University, and to the sub-chief examiners of my doctoral dissertation, Prof. Hideo Kubo, Prof. Jun Masamune, and Prof. Michiko Yuri.

I am grateful to all the members of Komatsuzaki Laboratory, especially Prof. Sosuke Ito for constant encouragement and highly constructive discussions. It was quite fortunate that I was in the same laboratory with him even though only in the last one year of my research life. I would also like to thank Dr. Yutaka Nagahata in Johns Hopkins University, an old member of the laboratory who has advised me a lot since the time even before I came to Hokkaido University. I would also like to thank all my friends in Hokkaido University, especially my colleagues Dr. Dai Akita and Mr. Ryosuke Tanaka, and friends and researchers who I met at research meetings and Society of Young Scientists in Biophysics.

I would also like to thank Dr. Satoru Tsugawa in RIKEN, who was also an old member of Komatsuzaki Laboratory at the same time, and all other old members of Aizawa Laboratory in Waseda University, where I started my research with them. Especially, I am grateful to my former colleagues Mr. Noi Takahashi in Osaka University and Mr. Hiroki Tanaka in the University of Tokyo. We shared the hard times and joys in Waseda University and encouraged each other even after graduation.

Finally, I would like to thank my family, who supported me mentally and financially. It is owing to their help and encouragement that I was able to continue my research life up to today.

Bibliography

1 H Noji, R Yasuda, M Yoshida, and K Kinosita. Direct observation of the rotation of F_1-ATPase. *Nature*, 386:299–302, 1997.

2 Ryohei Yasuda, Hiroyuki Noji, Kazuhiko Kinosita, and Masasuke Yoshida. F_1-ATPase is a highly efficient molecular motor that rotates with discrete 120 ° steps. *Cell*, 93(7):1117–1124, 1998.

3 Ei-ichiro Saita, Toshiharu Suzuki, Kazuhiko Kinosita, and Masasuke Yoshida. Simple mechanism whereby the F_1-ATPase motor rotates with near-perfect chemomechanical energy conversion. *Proceedings of the National Academy of Sciences*, page 201422885, 2015.

4 Shoichi Toyabe, Tetsuaki Okamoto, Takahiro Watanabe-Nakayama, Hiroshi Taketani, Seishi Kudo, and Eiro Muneyuki. Nonequilibrium Energetics of a Single F_1-ATPase Molecule. *Physical Review Letters*, 104(19):198103, 2010.

5 Eva Zimmermann and Udo Seifert. Efficiencies of a molecular motor: A generic hybrid model applied to the F 1-ATPase. *New Journal of Physics*, 14(10):103023, 2012.

6 Kyogo Kawaguchi, Shin Ichi Sasa, and Takahiro Sagawa. Nonequilibrium dissipation-free transport in F_1-ATPase and the thermodynamic role of asymmetric allosterism. *Biophysical Journal*, 106(11):2450–2457, 2014.

7 Kengo Adachi, Kazuhiro Oiwa, Takayuki Nishizaka, Shou Furuike, Hiroyuki Noji, Hiroyasu Itoh, Masasuke Yoshida, and Kazuhiko Kinosita. Coupling of Rotation and Catalysis in F_1-ATPase Revealed by Single-Molecule Imaging and Manipulation. *Cell*, 130(2):309–321, 2007.

8 Katsuya Shimabukuro, Ryohei Yasuda, Eiro Muneyuki, Kiyotaka Y Hara, Kazuhiko Kinosita, and Masasuke Yoshida. Catalysis and rotation of F_1 motor: cleavage of ATP at the catalytic site occurs in 1 ms before 40 degree substep rotation. *Proceedings of the National Academy of Sciences of the United States of America*, 100(25):14731–14736, 2003.

9 T Funatsu, Y Harada, M Tokunaga, K Saito, and T Yanagida. Imaging of single fluorescent molecules and individual ATP turnovers by single myosin molecules in aqueous solution., 1995.

10 Takayuki Nishizaka, Kazuhiro Oiwa, Hiroyuki Noji, Shigeki Kimura, Eiro Muneyuki, Masasuke Yoshida, and Kazuhiko Kinosita. Chemomechanical coupling in F_1-ATPase revealed by simultaneous observation of nucleotide kinetics and rotation. *Nature Structural & Molecular Biology*, 11(2):142–148, 2004.

11 Rikiya Watanabe, Ryota Iino, and Hiroyuki Noji. Phosphate release in F_1-ATPase catalytic cycle follows ADP release. *Nature Chemical Biology*, 6:814–820, 2010.

12 Rikiya Watanabe, Ryota Iino, Katsuya Shimabukuro, Masasuke Yoshida, and Hiroyuki Noji.

Temperature-sensitive reaction intermediate of F_1-ATPase. *EMBO reports*, 9(1):84–90, 2008.

13 Sawako Enoki, Rikiya Watanabe, Ryota Iino, and Hiroyuki Noji. Single-molecule study on the temperature-sensitive reaction of F_1-ATPase with a hybrid F_1 carrying a single β (E190D). *Journal of Biological Chemistry*, 284(34):23169–23176, 2009.

14 Rikiya Watanabe, Yoshihiro Minagawa, and Hiroyuki Noji. Thermodynamic analysis of F_1-ATPase rotary catalysis using high-speed imaging. *Protein Science*, 23(12):1773–1779, 2014.

15 Takayuki Uchihashi. High-Speed Atomic Force. *Science*, 333(August):755, 2011.

16 Ryota Iino and Hiroyuki Noji. Rotary catalysis of the stator ring of F_1-ATPase. *Biochimica et Biophysica Acta - Bioenergetics*, 1817(10):1732–1739, 2012.

17 Chun-Biu Li, Hiroshi Ueno, Rikiya Watanabe, Hiroyuki Noji, and Tamiki Komatsuzaki. ATP hydrolysis assists phosphate release and promotes reaction ordering in F_1-ATPase. *Nature Communications*, 6:10223, 2015.

18 H Eyring. The Activated Complex in Chemical Reactions. *The Journal of Chemical Physics*, 445:107 – 115, 1935.

19 M. G. Evans and M. Polanyi. Some Applications of the Transition State Method to the Calculation of Reaction Velocities, Especially in Solution. *Trans. Faraday Soc.*, 31:875, 1935.

20 Rikiya Watanabe, Daichi Okuno, Shouichi Sakakihara, Katsuya Shimabukuro, Ryota Iino, Masasuke Yoshida, and Hiroyuki Noji. Mechanical modulation of catalytic power on F_1-ATPase. *Nature Chemical Biology*, 8(1):86–92, 2011.

21 Rikiya Watanabe, Kumiko Hayashi, Hiroshi Ueno, and Hiroyuki Noji. Catalysis-enhancement via rotary fluctuation of F_1-atpase. *Biophysical Journal*, 105(10):2385–2391, 2013.

22 Robert Brown. On the particles contained in the pollen of plants; and on the general existence of active molecules in organic and inorganic bodies. *Edinburgh New Philosophical Journal*, 5:358–371, 1828.

23 A. Einstein. Über die von der molekularkinetischen Theorie der Wärme geforderte Bewegung von in ruhenden Flüssigkeiten suspendierten Teilchen. *Annalen der Physik*, 322(8):549–560, 1905.

24 Albert Einstein and Reinhold Fürth. *Investigations on the theory of Brownian movement*. Dover Publications, 1956.

25 Jean Perrin. Mouvement brownien et réalité moléculaire. In *Annales de Chimie et de Physique*, volume 18, pages 5–104, 1909.

26 Jean Perrin. *Les atomes*. Nouvelle collection scientifique. F. Alcan, 1914.

27 M C Wang and G E Uhlenbeck. On the theory of brownian motion II. *Reviews of Modern Physics*, 17:323–342, 1945.

28 S. Chandrasekhar. Stochastic Problems in Physics and Astronomy. *Reviews of Modern Physics*, 15(1):1–89, 1943.

29 Morikazu Toda and Kubo Ryogo. *Statistical Physics*. Springer-Verlag.

30 Robert Zwanzig. *Nonequilibrium statistical mechanics*. Oxford University Press, 2001.

31 Crispin W. Gardiner. *Stochastic methods : a handbook for the natural and social sciences*. Springer, 2009.

32 Paul Langevin. Sur la théorie du mouvement brownien *C. R. Acad. Sci. Paris.*

33 Don S. Lemons and Anthony Gythiel. Paul Langevin ' s 1908 paper ‘ ‘ On the Theory of Brownian Motion " & On the Theory of Brownian Motion, A note from M . P . Langevin, presented by M . Mascart . *American Journal of Physics*, 65(11):1079–1081, 1997.

34 Noam Agmon and J. J. Hopfield. Transient Kinetics of Chemical Reactions with Bounded Diffusion Perpendicular to the Reaction Coordinate: Intramolecular Processes with Slow Conformational Changes. *The Journal of Chemical Physics*, 78(1983):6947–6959, 1983.

35 Noam Agmon and J. J. Hopfield. CO binding to heme proteins: A model for barrier height distributions and slow conformational changes. *The Journal of Chemical Physics*, 79(4):2042–2053, 1983.

36 R. H. Austin, K. W. Beeson, L. Eisenstein, H. Frauenfelder, and I. C. Gunsalus. Dynamics of Ligand Binding to Myoglobin. *Biochemistry*, 14(24):5355–5373, 1975.

37 H.A. Kramers. Brownian motion in a field of force and the diffusion model of chemical reactions. *Physica*, 7(4):284–304, 1940.

38 Hitoshi Sumi and R. A. Marcus. Dynamical effects in electron transfer reactions. *The Journal of Chemical Physics*, 84(9):4896, 1986.

39 R Zwanzig. Rate processes with dynamical disorder. *Accounts of Chemical Research*, 23(5):148–152, 1990.

40 H P Lu, L Xun, and X S Xie. Single-molecule enzymatic dynamics. *Science*, 282(December):1877–1882, 1998.

41 Antoine M van Oijen, Paul C Blainey, Donald J Crampton, Charles C Richardson, Tom Ellenberger, and X Sunney Xie. Single-molecule kinetics of lambda exonuclease reveal base dependence and dynamic disorder. *Science*, 301(5637):1235–1238, 2003.

42 Brian P English, Wei Min, Antoine M van Oijen, Kang Taek Lee, Guobin Luo, Hongye Sun, Binny J Cherayil, S C Kou, and X Sunney Xie. Ever-fluctuating single enzyme molecules: Michaelis-Menten equation revisited. *Nature Chemical Biology*, 2(2):87–94, 2006.

43 Gregory K. Schenter, H. Peter Lu, and X. Sunney Xie. Statistical Analyses and Theoretical Models of Single-Molecule Enzymatic Dynamics. *The Journal of Physical Chemistry A*, 103:10477–10488, 1999.

44 Wei Min, X. Sunney Xie, and Biman Bagchi. Two-Dimensional Reaction Free Energy Surfaces of Catalytic Reaction: Effects of Protein Conformational Dynamics on Enzyme Catalysis. *The Journal of Physical Chemistry B*, 112(2):454–466, 2008.

45 Wei Min, X. Sunney Xie, and Biman Bagchi. Role of conformational dynamics in kinetics of an enzymatic cycle in a nonequilibrium steady state. *Journal of Chemical Physics*, 131(6), 2009.

46 Hans Philipp Lerch, Alexander S. Mikhailov, and Rudolf Rigler. Statistical tools for the detection of memory and conformational motions in single-enzyme kinetics. *Chemical Physics*, 331(2-3):304–308, 2007.

47 Tatyana G. Terentyeva, Hans Engelkamp, Alan E. Rowan, Tamiki Komatsuzaki, Johan Hofkens, Chun Biu Li, and Kerstin Blank. Dynamic disorder in single-enzyme experiments: Facts and artifacts. *ACS Nano*, 6(1):346–354, 2012.

48 Shou Furuike, Kengo Adachi, Naoyoshi Sakaki, Rieko Shimo-Kon, Hiroyasu Itoh, Eiro Muneyuki, Masasuke Yoshida, and Kazuhiko Kinosita. Temperature dependence of the rotation and hydrolysis

activities of F_1-ATPase. *Biophysical journal*, 95(2):761–770, 2008.

49 Mizuki Sekiya, Robert K. Nakamoto, Marwan K. Al-Shawi, Mayumi Nakanishi-Matsui, and Masamitsu Futai. Temperature dependence of single molecule rotation of the Escherichia coli ATP synthase F_1 sector reveals the importance of γ-β subunit interactions in the catalytic dwell. *Journal of Biological Chemistry*, 284(33):22401–22410, 2009.

50 Martin Karplus. Aspects of Protein Reaction Dynamics : Deviations from Simple Behavior. *Journal of Physical Chemistry B*, 104:11–27, 2000.

51 H Wang and G Oster. Energy transduction in the F_1 motor of ATP synthase. *Nature*, 396(6708):279–282, 1998.

52 Hongyun Wang. Several Issues in Modeling Molecular Motors. *Journal of Computational and Theoretical Nanoscience*, 5(12):2311–2345, 2008.

53 R Yasuda, H Noji, M Yoshida, K Kinosita, and H Itoh. Resolution of distinct rotational substeps by submillisecond kinetic analysis of F_1-ATPase. *Nature*, 410:898–904, 2001.

54 B. Efron and R. Tibshirani. [Bootstrap Methods for Standard Errors, Confidence Intervals, and Other Measures of Statistical Accuracy]: Rejoinder. *Statistical Science*, 1(1):77–77, 1986.

55 Thomas M. Cover and Joy A. Thomas. *Elements of Information Theory*. John Wiley and Sons, 2005.

56 E Yeramian and P Claverie. Analysis of multiexponential functions without a hypothesis as to the number of components. *Nature*, 326(6109):169–174, 1987.

57 Chun-Biu Li and Tamiki Komatsuzaki. Aggregated Markov Model Using Time Series of Single Molecule Dwell Times with Minimum Excessive Information. *Physical Review Letters*, 111(5):058301, 2013.

58 Kumiko Hayashi, Hiroshi Ueno, Ryota Iino, and Hiroyuki Noji. Fluctuation Theorem Applied to F_1-ATPase. *Physical Review Letters*, 104(21):218103, 2010.

59 Shoichi Toyabe, Takahiro Watanabe-Nakayama, Tetsuaki Okamoto, Seishi Kudo, and Eiro Muneyuki. Thermodynamic efficiency and mechanochemical coupling of F_1-ATPase. *Proceedings of the National Academy of Sciences of the United States of America*, 108(44):17951–6, 2011.

60 Howard Brenner. The slow motion of a sphere through a viscous fluid towards a plane surface. *Chemical Engineering Science*, 16(3-4):242–251, 1961.

61 Yuko Ito and Mitsunori Ikeguchi. Structual Fluctuation and Concerted Motions in F_1-ATPase: A Molecular Dynamics Study. *Journal of computational chemistry*, 31(16):2175–2185, 2010.

62 Rikiya Watanabe and Hiroyuki Noji. Characterization of the temperature-sensitive reaction of F_1-ATPase by using single-molecule manipulation. *Scientific Reports*, 4:4962, 2014.

63 D Truhlar and A Kohen. Convex Arrhenius plots and their interpretation. *Proc. Nat. Acad. Sci. USA*, 98:848–851, 2001.

64 T.-L. Kuo, S. Garcia-Manyes, J. Li, I. Barel, H. Lu, B. J. Berne, M. Urbakh, J. Klafter, and J. M. Fernandez. Probing static disorder in Arrhenius kinetics by single-molecule force spectroscopy. *Proceedings of the National Academy of Sciences*, 107(25):11336–11340, 2010.

65 D Beece, L Eisenstein, H Frauenfelder, D Good, M C Marden, L Reinisch, A H Reynolds, L B Sorensen, and K T Yue. Solvent viscosity and protein dynamics. *Biochemistry*, 19(23):5147–5157, 1980.

66 Anjum Ansari, Colleen M Jones, Eric R Henry, James Hofrichter, and William A Eaton. The Role of Solvent Viscosity in the Dynamics of Protein Conformational Changes. *Science*, 256(26):1796–1798, 1992.

67 K W Plaxco and D Baker. Limited internal friction in the rate-limiting step of a two-state protein folding reaction. *Proceedings of the National Academy of Sciences of the United States of America*, 95(23):13591–13596, 1998.

68 Stephen J Hagen. Solvent viscosity and friction in protein folding dynamics. *Current Protein & Peptide Science*, 11(5):385–395, 2010.

69 David de Sancho, Anshul Sirur, and Robert B Best. Molecular origins of internal friction effects on protein-folding rates. *Nature communications*, 5:4307, 2014.

70 Andrea Soranno, Andrea Holla, Fabian Dingfelder, Daniel Nettels, Dmitrii E. Makarov, and Benjamin Schuler. Integrated view of internal friction in unfolded proteins from single-molecule FRET, contact quenching, theory, and simulations. *Proceedings of the National Academy of Sciences*, page 201616672, 2017.

71 Yong Wang and Giovanni Zocchi. Elasticity of globular proteins measured from the ac susceptibility. *Physical Review Letters*, 105(23):238104, 2010.

72 Yong Wang and Giovanni Zocchi. The folded protein as a viscoelastic solid. *Europhysics Letters*, 96(1):18003, 2011.

73 Yong Wang and Giovanni Zocchi. Viscoelastic transition and yield strain of the folded protein. *PLoS ONE*, 6(12):e28097, 2011.

74 Hao Qu and Giovanni Zocchi. How enzymes work: A look through the perspective of molecular viscoelastic properties. *Physical Review X*, 3(1):1–10, 2013.

75 Amila Ariyaratne, Chenhao Wu, Chiao-Yu Tseng, and Giovanni Zocchi. Dissipative Dynamics of Enzymes. *Physical Review Letters*, 113(19):1–5, 2014.

76 E Muneyuki, Hiroyuki Noji, Toyoki Amano, Tomoko Masaike, and Masasuke Yoshida. F_oF_1-ATP synthase: General structural features of 'ATP-engine' and a problem on free energy transduction. *Biochimica et Biophysica Acta - Bioenergetics*, 1458(2-3):467–481, 2000.

77 戸田盛和, 久保亮五, 橋爪夏樹, 斎藤信彦. 講座 現代物理学の基礎 [第 2 版] 5 統計物理学. 岩波書店, 1978.

78 Dmitrii E. Makarov. Interplay of non-Markov and internal friction effects in the barrier crossing kinetics of biopolymers: Insights from an analytically solvable model. *Journal of Chemical Physics*, 138(1), 2013.

79 S. C. Kou and X. Sunney Xie. Generalized langevin equation with fractional gaussian noise: Subdiffusion within a single protein molecule. *Physical Review Letters*, 93(18):1–4, 2004.

80 K Kinosita, R Yasuda, H Noji, and K Adachi. A rotary molecular motor that can work at near 100% efficiency. *Philosophical transactions of the Royal Society of London. Series B, Biological sciences*, 355:473–489, 2000.

81 Sosuke Ito and Takahiro Sagawa. Maxwell's demon in biochemical signal transduction. *Nature Communications*, 6(May):12, 2015.

82 Peixuan Guo, Hiroyuki Noji, Christopher M Yengo, Zhengyi Zhao, and Ian Grainge. Biological Nanomotors with a Revolution, Linear, or Rotation Motion Mechanism. *Microbiology and Molecular*

Biology Reviews, 80(1):161–186, 2016.

83 Yoshihiro Minagawa, Hiroshi Ueno, Mayu Hara, Yoshiko Ishizuka-Katsura, Noboru Ohsawa, Takaho Terada, Mikako Shirouzu, Shigeyuki Yokoyama, Ichiro Yamato, Eiro Muneyuki, Hiroyuki Noji, Takeshi Murata, and Ryota Iino. Basic properties of rotary dynamics of the molecular motor enterococcus hirae V_1-ATPase. *Journal of Biological Chemistry*, 288(45):32700–32707, 2013.

84 Hiroshi Ueno, Yoshihiro Minagawa, Mayu Hara, Suhaila Rahman, Ichiro Yamato, Eiro Muneyuki, Hiroyuki Noji, Takeshi Murata, and Ryota Iino. Torque Generation of Enterococcus hirae V-ATPase. *The Journal of biological chemistry*, 289(45):31212–23, 2014.

85 Jonathon Howard. *Mechanics of motor proteins and the cytoskeleton*. Sinauer Associates, Publishers, 2001.

86 Ken Sekimoto. *Stochastic energetics*. Springer, 2010.

87 関本謙. ゆらぎのエネルギー論. 岩波書店, 2004.

88 G E Uhlenbeck and L S Ornstein. On the theory of the Brownian motion. *Physical Review*, 36:823–841, 1930.

89 三井 斌友, 小藤 俊幸, 齊藤 善弘. 微分方程式による計算科学入門. 共立出版, 2004.

90 Peter E Kloeden and Eckhard. Platen. *Numerical solution of stochastic differential equations*. Springer-Verlag, 1995.